View metadata, citation and similar papers at core.ac.uk

brought to you by CORE

provided by NASA Technical Reports Server

N95-23193

43608

51P

NASA Contractor Report 195050

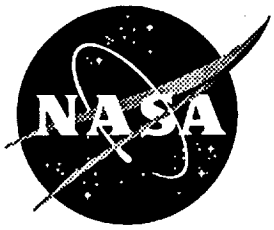

An Approximate Theoretical Method for Modeling the Static Thrust Performance of Non-axisymmetric Two-Dimensional Convergent-Divergent Nozzles

Craig A. Hunter
George Washington University
Joint Institute for Advancement of Flight Sciences
Langley Research Center, Hampton, Virginia

(NASA-CR-195050) AN APPROXIMATE THEORETICAL METHOD FOR MODELING THE STATIC THRUST PERFORMANCE OF NON-AXISYMMETRIC TWO-DIMENSIONAL CONVERGENT-DIVERGENT NOZZLES M.S. Thesis - George Washington Univ. (Joint Inst. for Advancement of Flight Sciences) 51 p

N95-23193

Unclas

G3/02 0043608

Cooperative Agreements NCC1-14 and NCC1-24

March 1995

National Aeronautics and
Space Administration
Langley Research Center
Hampton, Virginia 23681-0001

Abstract

An analytical/numerical method has been developed to predict the static thrust performance of non-axisymmetric two-dimensional convergent-divergent exhaust nozzles. Thermodynamic nozzle performance effects due to over- and underexpansion are modeled using one-dimensional compressible flow theory. Boundary layer development and skin friction losses are calculated using an approximate integral momentum method based on the classic Kármán-Polhausen solution. Angularity effects are included with these two models in a computational Nozzle Performance Analysis Code, NPAC. In four different case studies, results from NPAC are compared to experimental data obtained from subscale nozzle testing to demonstrate the capabilities and limitations of the NPAC method. In several cases, the NPAC prediction matched experimental gross thrust efficiency data to within 0.1 percent at a design NPR, and to within 0.5 percent at off-design conditions.

Table of Contents

Introduction

Supersonic cruise transport aircraft and modern fighter aircraft with supersonic cruise and dash capabilities use convergent-divergent (CD) exhaust nozzles to attain supersonic jet velocities necessary for flight in the high speed regime. Over the past several decades, propulsion nozzle research has led to the development of multi-mission supersonic exhaust nozzles that can provide efficient operation and meet varying requirements over an extended flight regime. For example, at supersonic cruise, where the ratio of lift to drag is low and fuel consumption is high [1], the exhaust nozzle must adjust its area ratio to fully expand engine flow and provide the optimum external geometry for low drag. For takeoff, climb to cruise, and air to air combat maneuvers, the exhaust nozzle will need to adjust for rapid changes in engine pressure ratio and accommodate high mass flow afterburning settings. Finally, the nozzle may be required to vector or reverse thrust, suppress jet noise, or maintain a low-observable, compact profile with a minimum effect on radar cross section and low IR emission.

Because of these diverse requirements, exhaust nozzle design is an integrated, multi-faceted effort, and is one of the most important technologies involved in the development of a supersonic aircraft. As such, an understanding of the flow physics and performance characteristics of CD exhaust nozzles is critical from experimental, theoretical, and computational standpoints. To meet this need, ongoing research efforts at NASA Langley Research Center are directed at generating an experimental database for new nozzle concepts [2], and developing, validating, and applying computational and analytical methods for the prediction of nozzle performance.

This paper provides a concise discussion of the basic flow physics, off-design operation, and thrust performance characteristics of convergent-divergent exhaust nozzles. As part of this discussion, a detailed thermodynamic thrust performance model is developed over the practical range of nozzle operation, and an approximate integral momentum boundary layer method is derived from first principles to calculate boundary layer development and skin friction losses. These models were combined with geometric loss estimates to develop a computational thrust performance prediction method for two-dimensional CD nozzles. A comparison of computational results with experimental data is presented for several test cases and gives valuable insights into the nozzle performance characteristics discussed as well as illustrating the applications and limits of the prediction method.

Nomenclature

Symbols

a	Speed of sound
α	Nozzle flap divergence angle
A	1D flow area
A^*	1D sonic flow area
A_9/A_8	Nozzle expansion ratio
B	Local nozzle wetted perimeter
C_f	Flat plate skin friction coefficient
$C_{F\eta}$	Thrust efficiency coefficient, $C_{F\eta}=F/F_i$
C_{FG}	Gross thrust efficiency coefficient
C_p	Specific heat at constant pressure
C_v	Specific heat at constant volume
δ	Boundary layer thickness
δ^*	Boundary layer displacement thickness
D	Internal nozzle skin friction drag
ΔC_{FG}	Gross thrust efficiency loss decrement, $\Delta C_{FG}\geq 0$
f	Boundary layer development function, $f=f(x)$
F	Fixed geometry nozzle thrust
F_i	Fully expanded, ideal variable geometry nozzle thrust
F_{ci}	Ideal convergent nozzle thrust
$\hat{F}$	Normalized thrust, $\hat{F}=F/P_{07}A_8$
ϕ	Nozzle divergence angular coordinate
g	Boundary layer development function, $g=g(x, NPR)$
γ	Specific heat ratio, $\gamma=C_p/C_v$
H_1	Boundary layer shape factor, $H_1=\delta^*/\theta$
H_2	Boundary layer shape factor, $H_2=\delta/\theta$
λ	Boundary layer development function, $\lambda=\lambda(x)$
$\dot{m}$	Mass flow rate
μ	Dynamic viscosity at static temperature
μ_0	Dynamic viscosity at stagnation temperature
M	Mach number
$\tilde{M}$	Boundary layer Mach number
M^*	Sonic Mach number, $M^*=1$
ν	Kinematic viscosity

P	Freestream static pressure
P_0	Stagnation pressure
θ	Boundary layer momentum thickness
Θ	Power function of θ, $\Theta=\theta^{5/4}$
r	Boundary layer temperature recovery factor
R	Ideal gas constant, $R=C_p-C_v$
Re	Reynolds number
ρ	Density
$\tilde{\rho}$	Boundary layer density
ρ^*	Sonic density
ΔS	Entropy rise
σ	Skin friction coefficient compressibility factor
τ_o	Flat plate shear stress
T	Freestream static temperature, absolute scale
T_0	Stagnation temperature, absolute scale
$\tilde{T}$	Boundary layer temperature, absolute scale
u	Boundary layer inner velocity
U	1D flow velocity, boundary layer outer velocity
U^*	Sonic velocity
ω	Boundary layer viscosity power law exponent
x	Curvilinear wall coordinate
y	Wall normal curvilinear coordinate

Subscripts

1C	First critical (Choke)
2C	Second critical
D	Design
SE	Shock at exit
7, 8, 9	Nozzle reservoir, throat, exit stations
∞	Ambient
α	Angularity effect
f	Friction effect
p	Pressure
v	Momentum
w	Wall (y=0)

Abbreviations

Axi	Axisymmetric
CD	Convergent-Divergent
NPAC	Nozzle Performance Analysis Code
NPR	Nozzle Pressure Ratio, $NPR=P_{07}/P_{\infty}$
1D	One-Dimensional
2D	Two-Dimensional

Convergent-Divergent Nozzle Thrust Performance Characteristics

The control volume used to calculate nozzle thrust is shown in Figure 1. Written in the streamwise direction, the steady flow control volume equation for conservation of impulse and momentum states that

$$\sum \text{Forces} = \dot{m}(U_{out} - U_{in}) \tag{1}$$

Figure 1: Nozzle Thrust Control Volume

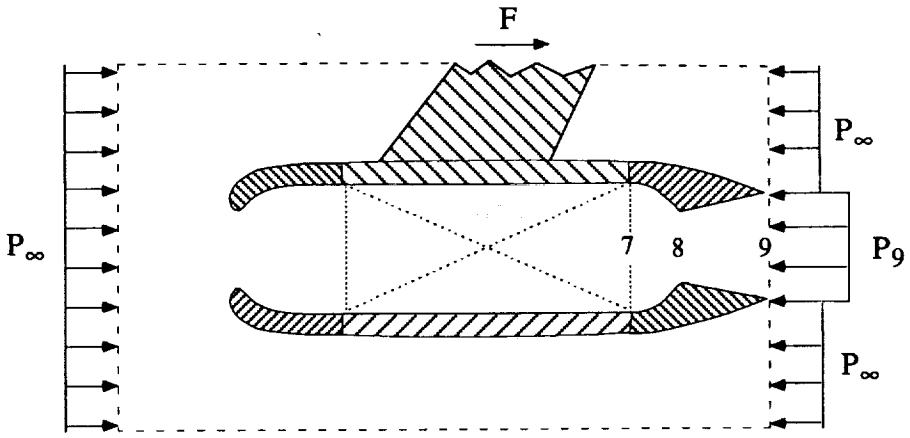

For the control volume shown, with pressures written relative to ambient and zero freestream velocity (static conditions),

$$F - (P_9 - P_\infty)A_9 = \dot{m}U_9 \tag{2}$$

So, net thrust is a combination of momentum and pressure thrust at the nozzle exit:

$$\begin{aligned} F &= \dot{m}U_9 + (P_9 - P_\infty)A_9 \\ &= F_v + F_p \end{aligned} \tag{3}$$

Now, with mass flow at the nozzle exit defined as

$$\dot{m}_9 = \rho_9 A_9 U_9 \tag{4}$$

and with the introduction of the ideal gas law,

$$P_9 = \rho_9 R T_9 \tag{5}$$

the nozzle mass flow is given by

$$\dot{m}_9 = \left(\frac{P_9}{RT_9}\right) A_9 U_9 \tag{6}$$

Substitution of (6) into (3) nets

$$F = \left(\frac{P_9}{RT_9}\right) A_9 U_9^2 + (P_9 - P_\infty) A_9 \tag{7}$$

But,

$$U_9 = M_9 a_9 = M_9 \sqrt{\gamma R T_9} \tag{8}$$

and the thrust equation becomes

$$F = \gamma P_9 A_9 M_9^2 + (P_9 - P_\infty) A_9 \tag{9}$$

Next,

$$P_9 = \left(\frac{P_9}{P_{07}}\right) P_{07} \tag{10}$$

$$P_\infty = \left(\frac{P_\infty}{P_{07}}\right) P_{07} \tag{11}$$

$$A_9 = \left(\frac{A_9}{A_8}\right) A_8 \tag{12}$$

so that

$$F = (P_{07} A_8) \frac{A_9}{A_8} \left[\gamma M_9^2 \left(\frac{P_9}{P_{07}}\right) + \left(\frac{P_9}{P_{07}} - \frac{P_\infty}{P_{07}}\right)\right] \tag{13}$$

When divided by $P_{07}A_8$, equation (13) yields a normalized thrust

$$\hat{F} = \frac{F}{P_{07} A_8} = \frac{A_9}{A_8} \left[\gamma M_9^2 \left(\frac{P_9}{P_{07}}\right) + \left(\frac{P_9}{P_{07}} - \frac{P_\infty}{P_{07}}\right)\right] \tag{14}$$

Now, with Station 7 at the reservoir, the following can be written

$$\frac{P_\infty}{P_{07}} = \frac{1}{NPR} \tag{15}$$

where NPR is the nozzle pressure ratio, or the ratio of reservoir stagnation pressure to exit back pressure. Furthermore,

$$\frac{P_9}{P_{07}} = \frac{P_\infty}{P_{07}} \frac{P_9}{P_\infty} = \frac{1}{NPR} \left(\frac{P_9}{P_\infty}\right) \tag{16}$$

With the substitution of these definitions and algebraic relations into (14), the control volume equation for normalized nozzle thrust looks as follows:

$$\hat{F} = \frac{F}{P_{07}A_8} = \frac{A_9}{A_8}\left[\frac{\gamma M_9^2}{NPR}\left(\frac{P_9}{P_\infty}\right) + \frac{1}{NPR}\left(\frac{P_9}{P_\infty} - 1\right)\right] \tag{17}$$

From this equation, the normalized momentum and pressure thrusts can be identified as:

$$\hat{F}_v = \frac{F_v}{P_{07}A_8} = \frac{A_9}{A_8}\left[\frac{\gamma M_9^2}{NPR}\left(\frac{P_9}{P_\infty}\right)\right] \tag{18}$$

$$\hat{F}_p = \frac{F_p}{P_{07}A_8} = \frac{A_9}{A_8}\left[\frac{1}{NPR}\left(\frac{P_9}{P_\infty} - 1\right)\right] \tag{19}$$

Equations (17) - (19) can be written as functions of NPR and nozzle geometry alone, but for now these equations are in a good form to discuss the thrust performance characteristics of convergent-divergent (CD) nozzles. Figure 2 shows a plot of normalized nozzle thrust vs. nozzle pressure ratio for a typical fixed geometry CD nozzle and a variable geometry CD nozzle at static conditions. The variable geometry nozzle changes expansion ratio with NPR such that exit flow is always fully expanded (i.e., $P_9=P_\infty$) and thrust is entirely due to momentum. The fixed geometry nozzle is shown to have a lower normalized static thrust over the entire NPR range except at the design point ($NPR=NPR_D$), where $P_9=P_\infty$ and fully expansion is attained.

Figure 2: Normalized Static Thrust vs. NPR

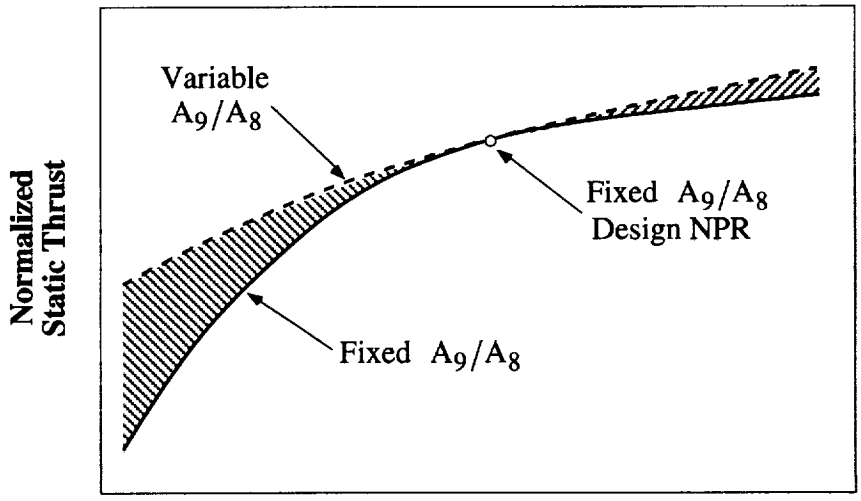

Figure 3: Nozzle Thrust Efficiency vs. NPR

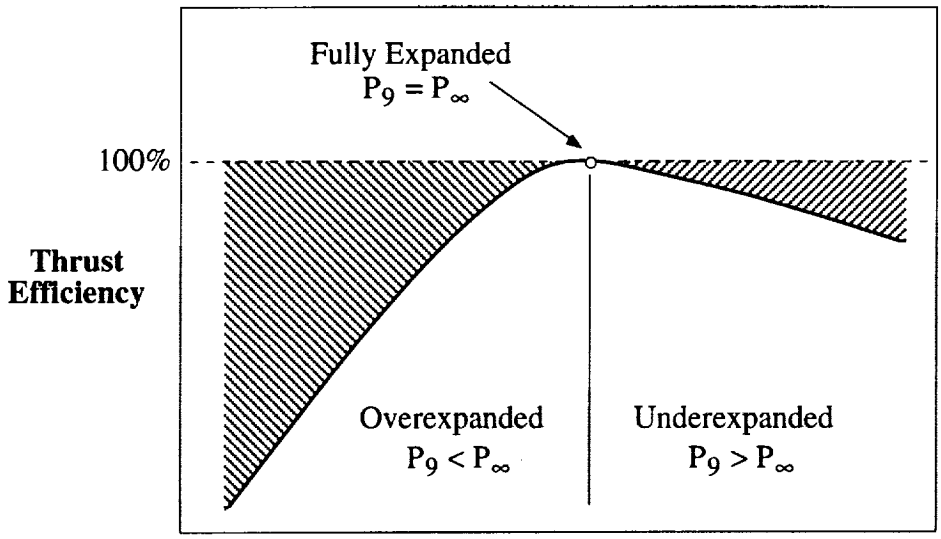

A measure of nozzle "thrust efficiency" can be obtained by dividing the normalized fixed geometry nozzle thrust ($\hat{F}$) by the normalized variable geometry nozzle thrust ($\hat{F}_i$). Such a measure is shown in Figure 3, and more clearly illustrates the performance regimes of a fixed geometry CD nozzle. At the design nozzle pressure ratio, nozzle exit pressure is equal to ambient pressure, and flow is supersonic and fully expanded. At off-design conditions above the design pressure ratio, the CD nozzle enters the underexpanded regime where exit pressure is higher than ambient pressure. In this regime, the fixed geometry expansion ratio (A_9/A_8) is lower than the ideal expansion ratio. The nozzle is physically too small for full internal expansion, and flow must expand to ambient pressure outside the nozzle as shown in Figure 4. This external, unducted expansion corresponds to a loss of thrust efficiency.

Figure 4: Underexpanded Nozzle Flow

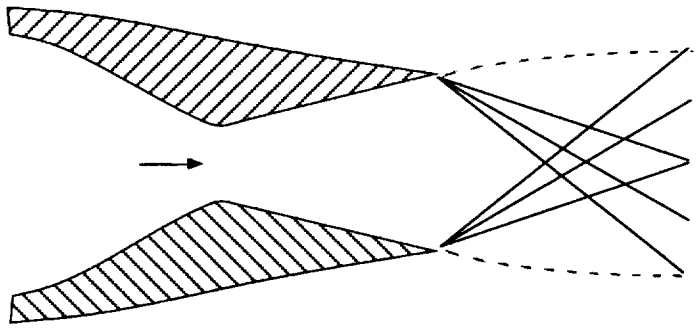

Below the design pressure ratio, the CD nozzle enters the overexpanded regime. In this off-design regime, the fixed geometry expansion ratio is too large for complete expansion to occur at any given NPR. To satisfy pressure boundary conditions in the reservoir and at the nozzle exit, flow must recompress. At nozzle pressure ratios immediately below design, nozzle exit pressure is lower than ambient pressure, and recompression occurs outside the nozzle through a series of shock and expansion fan "cells", shown in Figure 5. This irreversible compression mechanism is responsible for the loss in thrust efficiency shown in Figure 3, and defines the off-design "externally overexpanded" regime.

Figure 5: External Overexpansion

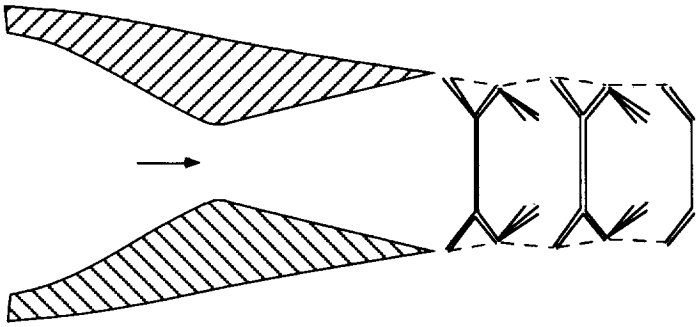

Farther below the design pressure ratio, the nozzle expansion ratio is too large for even internal expansion to persist, and recompression occurs in the nozzle divergent section through a standing normal shock as shown in Figure 6. While this regime still contains overexpanded flow, overexpansion occurs inside the nozzle only; flow downstream of the normal shock is subsonic, and nozzle flow can adjust to ambient pressure at the nozzle exit. This regime is known as the internally overexpanded or "shock" regime, and occurs between the choke or first critical nozzle pressure ratio (NPR_{1C}) and the second critical nozzle pressure ratio (NPR_{2C}), where the shock is at the nozzle exit.

Figure 6: Internal Overexpansion

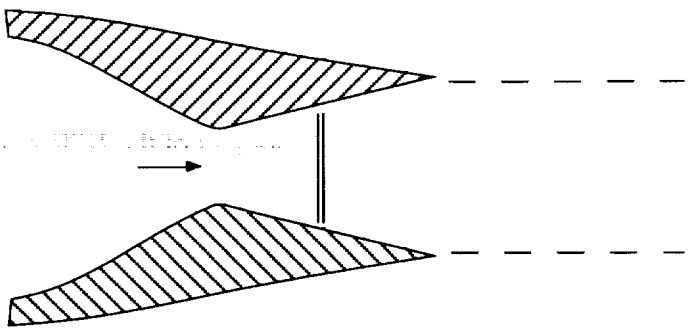

As indicated in Figure 3, thrust efficiency decreases at a greater rate below the design NPR of a nozzle. For externally overexpanded flow ($P_9<P_\infty$), equation (19) shows that pressure thrust is negative; i.e., low pressure acting on the nozzle exit creates a drag. In addition, pressures along downstream portions of the nozzle divergent walls will be less than ambient, creating an internal pressure drag. For the case of internally overexpanded shock regime flow, exit pressure equals ambient pressure, but pressures on the nozzle divergent walls are still lower than ambient and there is still an internal drag. More importantly, though, the nozzle also has a subsonic exit velocity and momentum thrust is significantly reduced.

Figure 7: Critical NPR's vs. Expansion Ratio

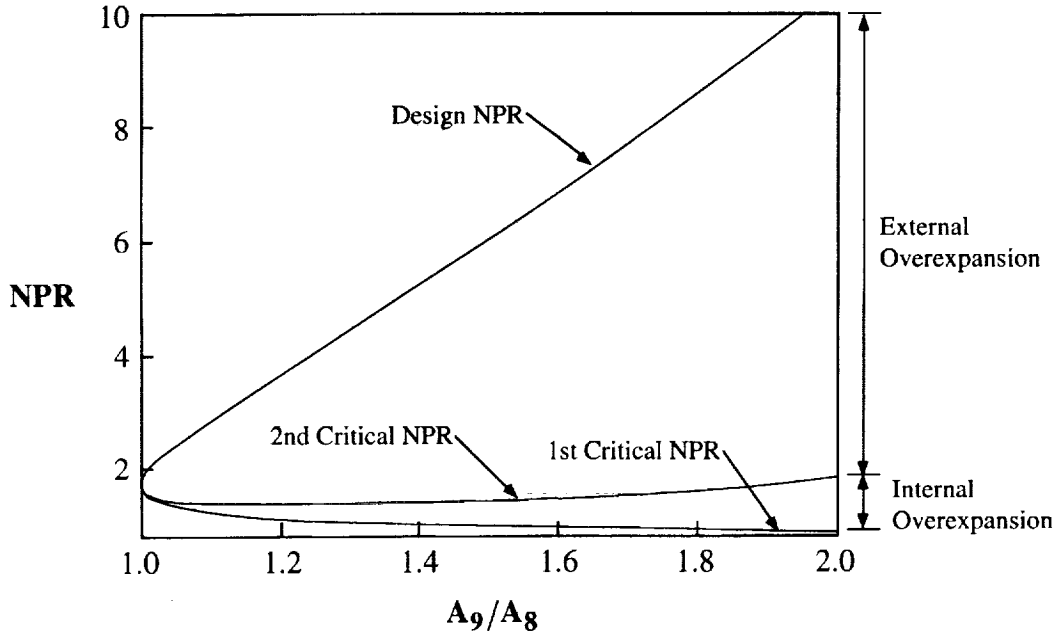

Figure 7 shows the first and second critical pressure ratios and the design pressure ratio plotted against nozzle expansion ratio for the 1D, adiabatic, inviscid flow of air with a specific heat ratio γ=1.4. The 1D approximation shows that the shock regime occurs over a very small NPR range, and implies that the majority of thrust efficiency drop-off below the design NPR occurs in the externally overexpanded regime. In reality this is not usually the case, and the shock regime encompasses a significant part of the NPR range below design.

Growth of the shock regime is the result of shock induced boundary layer separation in the divergent section of the nozzle, illustrated in Figure 8. The predominant effect of this separation is a reduction in subsonic pressure recovery past the shock. Since exit pressure is fixed at ambient, the loss in pressure recovery results in higher than normal pressures inside the nozzle divergent section. The nozzle shock will compensate for this by moving upstream of its normal (unseparated) location and decreasing in strength. For every increasing NPR in the shock regime, then, separation causes a lag in nozzle performance by delaying downstream movement of the nozzle shock. This results in an extended shock regime and a shifted, higher second critical NPR. For convenience, the shifted second critical NPR will be denoted as the "shock at exit" NPR, or NPR_{SE}. It is important to note that the design NPR of a nozzle is independent of off-design, internal behavior, and so a fixed design NPR and an extended shock regime result in a smaller externally overexpanded regime.

Figure 8: CD Nozzle with Shock Induced Boundary Layer Separation

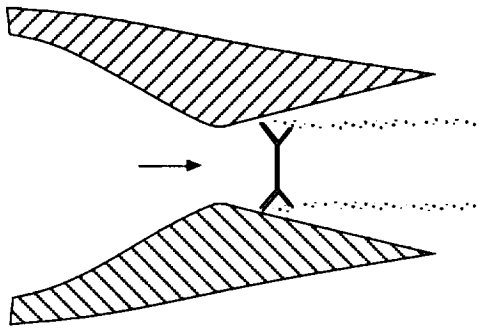

In most cases, the major effect of boundary layer separation in a fluid dynamic system is the resulting change in the system geometry caused by the separation. Translated to a CD nozzle, this implies that shock induced boundary layer separation delays operating points of a nozzle by changing the effective nozzle geometry. This is most evident in the extreme case of a nozzle with fully detached shock induced boundary layer separation, leading to an important analogy shown in Figure 9 which states that the separation point becomes the effective exit of a new, lower expansion ratio nozzle. At each NPR, then, the separated nozzle behaves like a shorter, lower expansion ratio nozzle with a shock at its exit. Thus, the nozzle will pass through the shock regime as a series of smaller nozzles operating at their "shock at exit" NPR's. The sum of the infinite number of individual smaller shifts forms a cumulative shift and determines the actual NPR_{SE}.

Figure 9: Separated CD Nozzle Expansion Ratio Analogy

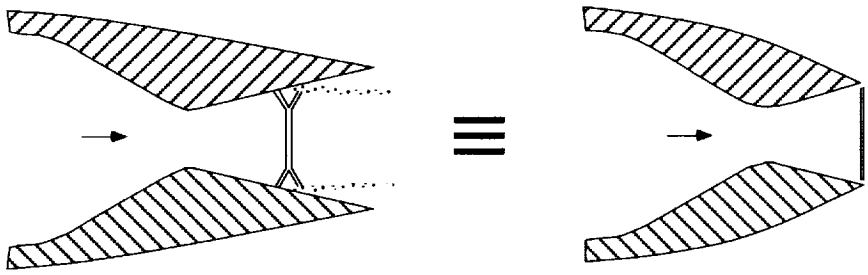

As discussed, overexpansion occurs because the nozzle expansion ratio is too large to maintain full expansion for a given NPR. In essence, then, separation becomes a "variable geometry" mechanism by which nozzle flow adjusts to a smaller, more correct expansion ratio. As might be expected, the most notable result of this separation geometry adjustment is an increase in static thrust efficiency, shown in Figure 10. This increase is the result of the natural tendency of an overexpanded fluid stream to reach a more efficient balance between internal energy and momentum, which translates into more efficient expansion and better conversion of total pressure and temperature into momentum and thrust. In addition, separation and the associated loss in pressure recovery past the separation point result in higher static pressures on the nozzle divergent flaps, reducing the internal drag discussed previously. In the limiting case of full detachment and zero pressure recovery past the shock, pressures all along the divergent walls will be equal to ambient pressure and the drag force will be eliminated.

Figure 10: Separation Effects on Thrust Performance

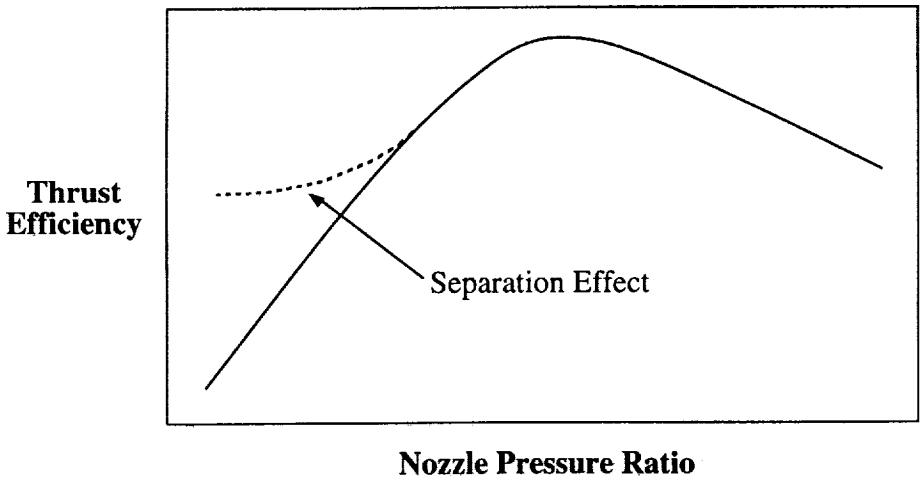

Though separation can be desirable for improving static thrust efficiency, the stability of shock - boundary layer interaction and corresponding separation is unpredictable in most cases, and this gives rise to serious design concerns. Asymmetric, unsteady, or transitory separation can have a detrimental or even catastrophic effect on almost any fluid machinery device, causing flow vectoring, pressure pulsations, and oscillatory flow patterns. In addition, though stable separation increases the static thrust performance of CD nozzles, wind-on aeropropulsive performance may suffer. Internal separation in a fixed geometry CD nozzle can increase the effective base area of an aircraft afterbody and couple with external separation to pump down aft facing surfaces, increasing afterbody drag. Thus, while static nozzle thrust efficiency increases, aeropropulsive "thrust minus drag" efficiency decreases, and a net performance decrease is realized.

Gas Dynamic Modeling

To write normalized thrust as a function of NPR, exit Mach number and exit pressure ratio (P_9/P_∞) must be known as functions of NPR. To determine these variables, nozzle performance will be divided into two NPR ranges:

Low End	$\{NPR_{1C} \le NPR \le NPR_{2C}\}$
High End	$\{NPR \ge NPR_{2C}\}$

Recall that the first critical pressure ratio (NPR_{1C}) is the point at which the nozzle chokes, and the second critical pressure ratio (NPR_{2C}) is the limiting point in the internally overexpanded regime at which a shock is at the nozzle exit. This second critical pressure ratio refers to an "ideal" case, and not the separation shifted, "shock at exit" NPR.

Proceeding with the analysis, the first and second critical pressure ratios can be determined with 1D flow relations as follows. First, knowing $P_9=P_\infty$ at the first critical pressure ratio, a simple algebraic relation can be written

$$\frac{1}{NPR_{1C}} = \frac{P_\infty}{P_{07}} = \frac{P_9}{P_{07}} = \frac{P_9}{P_{09}}\frac{P_{09}}{P_{07}} \tag{20}$$

Now, since nozzle flow is isentropic at the first critical pressure ratio, $P_{09}=P_{07}$, and

$$\frac{1}{NPR_{1C}} = \frac{P_9}{P_{09}} \tag{21}$$

In terms of local pressure ratio, the area - Mach number relation is [3]

$$\frac{A}{A^*}=\frac{\left(\frac{\gamma-1}{2}\right)^{1/2}\left(\frac{2}{\gamma+1}\right)^{\frac{\gamma+1}{2(\gamma-1)}}}{\left[1-\left(\frac{P}{P_0}\right)^{\frac{\gamma-1}{\gamma}}\right]^{1/2}\left(\frac{P}{P_0}\right)^{\frac{1}{\gamma}}} \tag{22}$$

With $A/A^*=A_9/A_8$, and after substitution of (21), the area - Mach number relation becomes

$$\frac{A_9}{A_8}=\frac{\left(\frac{\gamma-1}{2}\right)^{1/2}\left(\frac{2}{\gamma+1}\right)^{\frac{\gamma+1}{2(\gamma-1)}}}{\left[1-\left(\frac{1}{NPR_{1C}}\right)^{\frac{\gamma-1}{\gamma}}\right]^{1/2}\left(\frac{1}{NPR_{1C}}\right)^{\frac{1}{\gamma}}} \tag{23}$$

For air with a specific heat ratio $\gamma=1.4$, equation (23) can be solved for $NPR_{1C}\leq 1.89$ to give the choke nozzle pressure ratio. Though not important at the moment, the design NPR of the nozzle (NPR_D) can also be determined from (23), since the design point fulfills the isentropic requirements of the choke point math model (20, 21). For the design condition, however, (23) must be solved for $NPR_D>1.89$. This double solution corresponds to subsonic and supersonic solutions of the area - Mach number relation.

Along these same lines, the second critical pressure ratio can be determined by coupling normal shock relations with the current math model. By denoting static and total pressure upstream of the shock as P and P_0 respectively, and the same downstream conditions as P' and P_0', the following algebraic expression can be written

$$\frac{P'}{P_{07}}=\frac{P'}{P}\frac{P}{P_0}\frac{P_0}{P_{07}} \tag{24}$$

Now, flow up to the shock is isentropic, so $P_0=P_{07}$. In addition, flow downstream of the shock is at ambient pressure, so $P'=P_\infty$. Keeping the static pressure ratio across the shock written as P'/P, and the static/total pressure ratio upstream of the shock as P/P_0,

$$\frac{P'}{P_{07}}=\frac{P_\infty}{P_{07}}=\frac{1}{NPR_{2C}}=\left(\frac{P'}{P}\right)\left(\frac{P}{P_0}\right)(1) \tag{25}$$

The static/total pressure ratio upstream of the shock corresponds to supersonic flow at the nozzle exit for the second critical and all subsequent nozzle pressure ratios, since exit Mach number of the nozzle remains constant above NPR_{2C}. The upshot of this relation is that the pressure ratio upstream of the shock is simply the inverse of the design NPR; i.e.,

$$\frac{P}{P_0} = \frac{1}{NPR_D} \tag{26}$$

and equation (25) reduces to the following:

$$\frac{1}{NPR_{2C}} = \left(\frac{P'}{P}\right)\left(\frac{1}{NPR_D}\right) \tag{27}$$

The static pressure ratio across the shock can be determined through a normal shock relation, where M is the Mach number upstream of the shock:

$$\frac{P'}{P} = \frac{2\gamma}{\gamma+1}M^2 - \left(\frac{\gamma-1}{\gamma+1}\right) \tag{28}$$

The upstream Mach number can be determined easily using a 1D relation [4] and equation (26).

$$\frac{1}{NPR_D} = \frac{P}{P_0} = \left[1 + \frac{\gamma-1}{2}M^2\right]^{-\frac{\gamma}{\gamma-1}} \tag{29}$$

Solving (29) for M^2 and substituting the resulting expression into (28) yields

$$\frac{P'}{P} = \frac{2\gamma}{\gamma+1}\left(\frac{2}{\gamma-1}\right)\left[\left(\frac{1}{NPR_D}\right)^{-\frac{\gamma-1}{\gamma}} - 1\right] - \left(\frac{\gamma-1}{\gamma+1}\right) \tag{30}$$

Finally, substituting (30) into (27) and performing some algebra results in

$$NPR_{2C} = NPR_D\left\{\frac{4\gamma}{(\gamma+1)(\gamma-1)}\left[NPR_D^{\frac{\gamma-1}{\gamma}} - 1\right] - \frac{\gamma-1}{\gamma+1}\right\}^{-1} \tag{31}$$

With the critical operating points of the nozzle defined, nozzle exit conditions can now be calculated, starting with the low end. The low end has already been defined as the internally overexpanded regime, and is characterized by a standing normal shock in the divergent section of the nozzle and subsonic velocity at the nozzle exit. In this regime, exit and ambient pressures are equal and thrust is entirely due to momentum. As such, the normalized static thrust equation reduces to the following:

$$\hat{F} = \frac{F}{P_{07}A_8} = \frac{A_9}{A_8}\left[\frac{\gamma M_9^2}{NPR}\right] \tag{32}$$

So, for the low end, only the exit Mach number must be determined. Knowing the nozzle has a choked throat, it follows that

$$A_8 = A_7^* \tag{33}$$

so that

$$\left(\frac{A_9}{A_8}\right)\left(\frac{P_9}{P_{07}}\right) = \left(\frac{A_9}{A_7^*}\right)\left(\frac{P_9}{P_{07}}\right) \tag{34}$$

For non-isentropic flow between any points 1 and 2 with no heat or work added [3]

$$\frac{\Delta S}{R} = \ln\left(\frac{P_{01}}{P_{02}}\right) \tag{35}$$

or,

$$\frac{P_{01}}{P_{02}} = e^{\Delta S/R} \tag{36}$$

In addition, the Area-Mach Number Relation looks as follows [4]:

$$\frac{A_2}{A_1} = \frac{M_1}{M_2}\left[\frac{1+\frac{\gamma-1}{2}M_2^2}{1+\frac{\gamma-1}{2}M_1^2}\right]^{\frac{\gamma+1}{2(\gamma-1)}} e^{\Delta S/R} \tag{37}$$

By substituting (36) into (37), an adiabatic, non-isentropic, no work flow relation is obtained for area, Mach number, and total pressure between any two points in flow:

$$\frac{A_2}{A_1} = \frac{M_1}{M_2}\left[\frac{1+\frac{\gamma-1}{2}M_2^2}{1+\frac{\gamma-1}{2}M_1^2}\right]^{\frac{\gamma+1}{2(\gamma-1)}} \frac{P_{01}}{P_{02}} \tag{38}$$

Now, A_2 could be thought of as a fictitious sonic point of A_9, and A_1 of A_7; i.e.,

$$A_2 = A_9^* \tag{39}$$

$$A_1 = A_7^* \tag{40}$$

From this definition, the following are true:

$$M_2 = M_9^* = 1 \tag{41}$$

$$M_1 = M_7^* = 1 \tag{42}$$

and,

$$P_{01} = P_{07} \tag{43}$$

$$P_{02} = P_{09} \tag{44}$$

When modified with these relations, equation (38) reduces to

$$\frac{A_9^*}{A_7^*} = \frac{P_{07}}{P_{09}} \tag{45}$$

or,

$$A_7^* = A_9^*\left(\frac{P_{09}}{P_{07}}\right) \tag{46}$$

So, by taking advantage of the sonic reference point concept, the area - Mach number relation (37) has been pared down to a simple expression relating sonic reference areas and total pressures. Now, (46) can be substituted directly into (34) which yields

$$\left(\frac{A_9}{A_8}\right)\left(\frac{P_9}{P_{07}}\right) = \left(\frac{A_9}{A_9^*}\right)\left(\frac{P_{07}}{P_{09}}\right)\left(\frac{P_9}{P_{07}}\right) \tag{47}$$

or,

$$\left(\frac{A_9}{A_8}\right)\left(\frac{P_9}{P_{07}}\right) = \left(\frac{A_9}{A_9^*}\right)\left(\frac{P_9}{P_{09}}\right) \tag{48}$$

Noting that

$$\frac{P_9}{P_{07}} = \frac{P_\infty}{P_{07}} = \frac{1}{NPR} \tag{49}$$

Equation (48) becomes

$$\left(\frac{A_9}{A_8}\right)\left(\frac{1}{NPR}\right) = \left(\frac{A}{A^*}\right)_9\left(\frac{P}{P_0}\right)_9 \tag{50}$$

For any point in compressible flow, isentropic 1D relations give [3]

$$\frac{A}{A^*} = \frac{1}{M}\left[\frac{2}{\gamma+1}\left(1+\frac{\gamma-1}{2}M^2\right)\right]^{\frac{\gamma+1}{2(\gamma-1)}} \tag{51}$$

$$\frac{P}{P_0} = \left[1+\frac{\gamma-1}{2}M^2\right]^{-\frac{\gamma}{\gamma-1}} \tag{52}$$

The product of the two relations in (51) and (52) looks as follows:

$$\left(\frac{A}{A^*}\right)\left(\frac{P}{P_0}\right) = \frac{1}{M}\left[\frac{2}{\gamma+1}\right]^{\frac{\gamma+1}{2(\gamma-1)}}\left[1+\frac{\gamma-1}{2}M^2\right]^{-1/2} \tag{53}$$

Substitution of (53) into (50) results in the following expression:

$$\left(\frac{A_9}{A_8}\right)\left(\frac{1}{NPR}\right) = \frac{1}{M_9}\left[\frac{2}{\gamma+1}\right]^{\frac{\gamma+1}{2(\gamma-1)}}\left[1+\frac{\gamma-1}{2}M_9^2\right]^{-1/2} \tag{54}$$

which can be written as

$$\frac{1}{M_9}\left[1+\frac{\gamma-1}{2}M_9^2\right]^{-1/2} = \left(\frac{A_9}{A_8}\right)\left(\frac{1}{NPR}\right)\left[\frac{2}{\gamma+1}\right]^{-\frac{\gamma+1}{2(\gamma-1)}} \tag{55}$$

Equation (55) can be rewritten as a quadratic equation for M_9^2 as follows:

$$\frac{\gamma-1}{2}\left[M_9^2\right]^2 + M_9^2 - \frac{1}{C^2} = 0 \tag{56}$$

where

$$C = \left(\frac{A_9}{A_8}\right)\left(\frac{1}{NPR}\right)\left[\frac{2}{\gamma+1}\right]^{-\frac{\gamma+1}{2(\gamma-1)}} \tag{57}$$

Using the quadratic formula, the solution of (56) for M_9^2 is

$$M_9^2 = -\frac{1}{\gamma-1} \pm \frac{1}{\gamma-1}\sqrt{1+4\left(\frac{\gamma-1}{2}\right)\left(\frac{1}{C^2}\right)} \tag{58}$$

By performing some algebra and knowing that M_9^2 must be positive, the end result is

$$M_9^2 = \frac{1}{\gamma - 1}\left[\sqrt{1 + \frac{2(\gamma - 1)}{C^2}} - 1\right] \tag{59}$$

Equation (59) can be substituted into (32) to net the complete low end normalized thrust equation

$$\hat{F} = \frac{F}{P_{07}A_8} = \frac{A_9}{A_8}\left(\frac{\gamma}{\gamma - 1}\right)\left(\frac{1}{NPR}\right)\left[\sqrt{1 + \frac{2(\gamma - 1)}{C^2}} - 1\right] \tag{60}$$

This analysis was performed with no reference to shock location or strength; shock losses were written in terms of an entropy rise and represented by a total pressure - area - Mach number relation. Determining the shock strength and location is a simple matter from this point. Denoting total pressure upstream of the shock as P_0 and downstream total pressure as P_0', the following can be written, since flow up to and past the shock is isentropic:

$$\frac{P_0'}{P_0} = \frac{P_{09}}{P_{07}} = \frac{P_{09}}{P_9}\frac{P_9}{P_{07}} = \frac{P_{09}}{P_9}\frac{P_\infty}{P_{07}} = \frac{P_{09}}{P_9}\left(\frac{1}{NPR}\right) \tag{61}$$

Substituting equation (52) for P_{09}/P_9 yields

$$\frac{P_0'}{P_0} = \left[1 + \frac{\gamma - 1}{2}M_9^2\right]^{\frac{\gamma}{\gamma - 1}}\left(\frac{1}{NPR}\right) \tag{62}$$

Once the total pressure ratio across the shock is determined, using (59) for M_9^2, the upstream Mach number can be found using a normal shock relation in the form [4]

$$\frac{P_0'}{P_0} = \left[\frac{\frac{\gamma + 1}{2}M^2}{1 + \frac{\gamma - 1}{2}M^2}\right]^{\frac{\gamma}{\gamma - 1}}\left[\frac{2\gamma}{\gamma + 1}M^2 - \frac{\gamma - 1}{\gamma + 1}\right]^{-\frac{1}{\gamma - 1}} \tag{63}$$

Finally, using (51) with $A^* = A_8$, the area at which the shock occurs is found as

$$A = \frac{A_8}{M}\left[\frac{2}{\gamma + 1}\left(1 + \frac{\gamma - 1}{2}M^2\right)\right]^{\frac{\gamma + 1}{2(\gamma - 1)}} \tag{64}$$

With knowledge of the nozzle geometry, the streamwise location of the shock can be determined from the shock area.

Now that the low end has been covered in detail, attention can turn to evaluating the high end. In this NPR range, the exit Mach number is constant and is the same as that at the second critical pressure ratio upstream of the exit shock. So, the remaining unknown in the normalized static thrust equation (17) is the exit pressure ratio, P_9/P_∞. This ratio can be determined as a simple function of NPR as follows. First, an algebraic relation can be written in the form

$$\frac{P_9}{P_\infty} = \frac{P_9}{P_{07}}\frac{P_{07}}{P_\infty} \tag{65}$$

Now, P_{07}/P_∞ is the NPR, and P_9/P_{07} is simply the pressure ratio corresponding to the exit Mach number. However, from (26), this ratio is known to be the inverse of the design NPR. Modified with this information, the relation is

$$\frac{P_9}{P_\infty} = \frac{1}{NPR_D}NPR = \frac{NPR}{NPR_D} \tag{66}$$

and the normalized high end thrust equation becomes

$$\hat{F} = \frac{F}{P_{07}A_8} = \frac{A_9}{A_8}\left[\frac{\gamma M_9^2}{NPR_D} + \left(\frac{1}{NPR_D} - \frac{1}{NPR}\right)\right] \tag{67}$$

Equation (29) can be used to give exit Mach number as a function of the design NPR. When substituted into (67), the resulting normalized high end thrust equation looks as follows:

$$\hat{F} = \frac{F}{P_{07}A_8} = \frac{A_9}{A_8}\left\{\left(\frac{2\gamma}{\gamma-1}\right)\left(\frac{1}{NPR_D}\right)\left[\left(\frac{1}{NPR_D}\right)^{-\frac{\gamma-1}{\gamma}} - 1\right] + \left[\frac{1}{NPR_D} - \frac{1}{NPR}\right]\right\} \tag{68}$$

From this equation, normalized momentum and pressure thrust can be identified as:

$$\hat{F}_v = \frac{F_v}{P_{07}A_8} = \frac{A_9}{A_8}\left(\frac{2\gamma}{\gamma-1}\right)\left(\frac{1}{NPR_D}\right)\left[\left(\frac{1}{NPR_D}\right)^{-\frac{\gamma-1}{\gamma}} - 1\right] \tag{69}$$

$$\hat{F}_p = \frac{F_p}{P_{07}A_8} = \frac{A_9}{A_8}\left[\frac{1}{NPR_D} - \frac{1}{NPR}\right] \tag{70}$$

Note that the normalized momentum thrust is simply a function of the nozzle geometry, i.e., A_9/A_8 and NPR_D, and does not change with NPR. Normalized pressure thrust, however, varies with NPR, subtracting from the momentum thrust for $NPR<NPR_D$ (overexpansion) and adding to the momentum thrust for $NPR>NPR_D$ (underexpansion).

The next step in this analysis is to determine the thrust of an ideal, fully expanded, variable expansion ratio nozzle such that a fixed geometry thrust efficiency can be defined, where the thrust efficiency coefficient is simply the ratio of normalized thrust to normalized ideal thrust:

$$C_{F\eta} = \frac{F}{F_i} = \frac{\left(\frac{F}{P_{07}A_8}\right)}{\left(\frac{F_i}{P_{07}A_8}\right)} = \frac{\hat{F}}{\hat{F}_i} \tag{71}$$

Going back to (17), with $P_9/P_\infty=1$ for fully expanded flow, the normalized thrust equation looks as follows, where F is replaced by F_i to denote the ideal, variable geometry nozzle thrust:

$$\frac{F_i}{P_{07}A_8} = \frac{A_9}{A_8}\left[\frac{\gamma M_9^2}{NPR}\right] \tag{72}$$

In this case, both the expansion ratio A_9/A_8 and exit Mach number are functions of NPR. For air with $\gamma=1.4$, equation (23) can be used to determine the design expansion ratio for any NPR above 1.89; for NPR's below 1.89, no "on-design" CD nozzle exists, and that range must be addressed separately. For now, however, the relation in (23) can be substituted into (72) to give

$$\hat{F}_i = \frac{F_i}{P_{07}A_8} = \left\{\frac{\left(\frac{\gamma-1}{2}\right)^{1/2}\left(\frac{2}{\gamma+1}\right)^{\frac{\gamma+1}{2(\gamma-1)}}}{\left[1-\left(\frac{1}{NPR}\right)^{\frac{\gamma-1}{\gamma}}\right]^{1/2}\left(\frac{1}{NPR}\right)^{\frac{1}{\gamma}}}\right\}\left[\frac{\gamma M_9^2}{NPR}\right] \tag{73}$$

Equation (29) can again be used to determine exit Mach number. When (29) is substituted into (73), the variable geometry normalized thrust equation becomes

$$\hat{F}_i = \frac{F_i}{P_{07}A_8} = \left[\frac{\left(\frac{\gamma-1}{2}\right)^{1/2}\left(\frac{2}{\gamma+1}\right)^{\frac{\gamma+1}{2(\gamma-1)}}}{\sqrt{1-\left(\frac{1}{NPR}\right)^{\frac{\gamma-1}{\gamma}}}}\right]\left[\frac{1}{NPR}\right]^{\frac{\gamma-1}{\gamma}}\left[\frac{2\gamma}{\gamma-1}\right]\left[\left(\frac{1}{NPR}\right)^{\frac{\gamma-1}{\gamma}}-1\right] \tag{74}$$

Because no "on-design" CD nozzle exists below NPR=1.89, a convergent nozzle must be used to determine an ideal nozzle thrust. In this case, the control volume model is still valid and simplified, since a convergent nozzle has an expansion ratio $A_9/A_8=1$. For the convergent nozzle, the normalized thrust equation looks as follows, where F_{ci} denotes the ideal convergent nozzle thrust:

$$\frac{F_{ci}}{P_{07}A_8} = \left[\frac{\gamma M_9^2}{NPR}\right] \tag{75}$$

For air with a specific heat ratio of $\gamma=1.4$, a convergent nozzle chokes at NPR=1.89. Below NPR=1.89 there is always subsonic flow and exit and ambient pressures are equal. In light of this, the simple 1D relation in (29) can be used to determine exit Mach number. Modified with this relation, the normalized convergent nozzle thrust equation becomes

$$\frac{F_{ci}}{P_{07}A_8} = \left[\frac{1}{NPR}\right]\left[\frac{2\gamma}{\gamma-1}\right]\left[\left(\frac{1}{NPR}\right)^{\frac{\gamma-1}{\gamma}}-1\right] \tag{76}$$

Now that the equations governing nozzle thrust performance over the low and high end regimes have been derived, it is important to note that, in most cases, the second critical NPR is so low that the low end regime need not be considered from a modeling standpoint. In addition, shock induced separation effects in a real nozzle dramatically alter and extend the low end regime into the NPR range where thermodynamics are governed by the high end model. Thus, for most nozzle applications, nozzle performance can be represented by high end thrust equations alone. Exceptions to this generalization are high expansion ratio nozzles with shallow divergence angles. Such nozzles have a wide, separation free low end regime and the second critical pressure ratio may fall into a range of practical interest.

Nozzle Thrust Performance: Loss Effects

The analysis performed thus far has resulted in a model for nozzle thrust efficiency based on the thermodynamics and gas dynamics of energy conversion in a fluid stream. Inefficiencies predicted by this model are not due to loss effects, but rather, are the physical thermodynamic result of expanding flow in a fixed geometry duct over a range of non-ideal pressure ratios. Since this model was developed assuming the 1D, adiabatic, isentropic flow of an ideal gas, real life departures from this ideal model are thereby due to non-1D and secondary flow effects, heat conduction effects, frictional and boundary layer effects, geometry induced loss mechanisms (internal wave radiation), and real gas effects.

Over the entire range of nozzle operation, loss effects cannot be modeled in a simple fashion. However, at the design point of the nozzle, flow is fully expanded and most closely resembles that predicted by the 1D model. At this condition, dominant loss effects can be readily and accurately predicted. As will be seen, losses calculated at the design NPR can be extended to other off-design, high end NPR's. Though such losses are not applicable to low end NPR's, this regime need not be modeled in most cases as discussed.

To include loss effects in the thermodynamic thrust performance model, it is first necessary to break nozzle thrust efficiency down into its momentum and pressure portions.

$$C_{F\eta} = \frac{F}{F_i} = \frac{F_v + F_p}{F_i} = \frac{\hat{F}_v + \hat{F}_p}{\hat{F}_i} \tag{77}$$

In a similar fashion, a gross thrust efficiency coefficient, that is, one that includes losses, can be defined, where the normalized momentum and pressure thrust with losses are denoted by primed quantities:

$$C_{FG} = \frac{\hat{F}'_v + \hat{F}'_p}{\hat{F}_i} \tag{78}$$

At the fully expanded design point of the nozzle (i.e., NPR=NPR_D) the following is true:

$$\hat{F}'_p = \hat{F}_p = 0 \tag{79}$$

$$C_{F\eta} = 1 \tag{80}$$

$$C_{FG} = C_{FG}^{pk} \tag{81}$$

where the peak gross thrust efficiency, C_{FG}^{pk}, is the ideal peak thrust efficiency of 1.0 minus losses at peak:

$$C_{FG}^{pk} = 1 - \Delta C_{FG}^{pk} \tag{82}$$

With these relations, the thrust efficiency and gross thrust efficiency equations become:

$$1 = \frac{\hat{F}_v}{\hat{F}_i} \tag{83}$$

$$C_{FG}^{pk} = \frac{\hat{F}'_v}{\hat{F}_i} \tag{84}$$

Combined, these two relations give

$$\hat{F}'_v = C_{FG}^{pk}\, \hat{F}_v \tag{85}$$

that is, the momentum thrust with losses is simply the ideal momentum thrust multiplied by the peak gross thrust efficiency. This result is of great importance, for it means that losses need only be predicted at the design point of the nozzle to model performance in the high end. Physically, this implies that nozzle losses affect only the momentum portion of normalized thrust, which was shown previously to be independent of NPR in the high end. From the peak gross thrust efficiency then, pressure thrust effects determine the actual thrust efficiency of the nozzle at each high end NPR. Thus, the peak gross thrust efficiency becomes the effective maximum thrust efficiency of the nozzle from which the thermodynamic model can predict over- and underexpansion inefficiencies at off-design high end NPR's. With these results, the gross thrust efficiency coefficient can be re-written as:

$$C_{FG} = \frac{C_{FG}^{pk}\, F_v + F_p}{F_i} \tag{86}$$

For comparison between the thermodynamic model and experimental data, a measured peak gross thrust efficiency can be inserted into equation (86). For an a priori performance prediction, however, the peak gross thrust efficiency must be determined by estimating the appropriate loss effects. The simplest such loss effect is angularity, which results from the non-1D flow of fluid at the nozzle exit. Angularity losses occur when the nozzle geometry generates non-axial jet velocities, as in the case of a nozzle with a non-zero exit divergence angle. For a fixed total thrust, components of momentum thrust generated in non-axial

directions will reduce the axial thrust of the nozzle, and a decrease in thrust efficiency is realized. For a 2D nozzle with a divergence half angle of α, the effects of angularity can be determined as follows.

Figure 11: Nozzle Divergence Polar Coordinate System

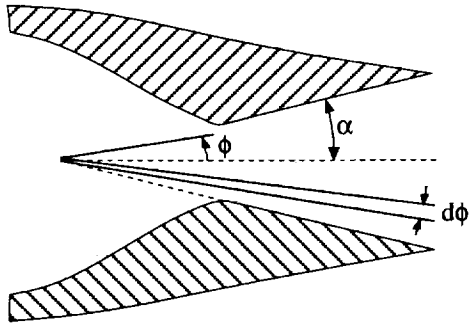

First, using a polar coordinate system originating from the vertex of the nozzle divergence angle as shown in Figure 11, the nozzle exit plane can be broken down into a series of streamtubes, each corresponding to a polar element $d\phi$. Each streamtube can then be thought of as containing an element of thrust dF_v of the total ideal momentum thrust F_v, where dF_v is defined as follows:

$$dF_v = F_v \frac{d\phi}{2\alpha} \tag{87}$$

The component of elemental momentum thrust in the axial direction, dF_{va}, is simply

$$dF_{va} = dF_v \cos\phi = \frac{F_v \cos\phi}{2\alpha} d\phi \tag{88}$$

It follows that the total axial thrust is simply the elemental axial thrusts integrated over the nozzle exit plane:

$$F_{va} = \int_{-\alpha}^{+\alpha} \frac{F_v \cos\phi}{2\alpha} d\phi$$

$$= \frac{F_v \sin\alpha}{\alpha} \tag{89}$$

Now, the gross thrust efficiency decrement due to angularity is:

$$\Delta C_{FG,\alpha} = \frac{F_v - F_{va}}{F_i} \tag{90}$$

but at the design NPR, $F_i=F_v$, and the decrement at peak is:

$$\Delta C_{FG,\alpha}^{pk} = 1 - \frac{F_{va}}{F_v} = 1 - \frac{\sin\alpha}{\alpha} \qquad \text{(2D Nozzle)} \quad (91)$$

Though not necessary for the current analysis, a similar derivation for an axisymmetric nozzle gives:

$$\Delta C_{FG,\alpha}^{pk} = \frac{1-\cos\alpha}{2} \qquad \text{(Axi Nozzle)} \quad (92)$$

The second loss effect that can be predicted in a nozzle is skin friction drag, though this loss effect requires a more rigorous analysis than angularity. The internal friction drag of the nozzle can be determined by integrating the product of the local skin friction coefficient, dynamic pressure, and wetted perimeter over the nozzle streamwise length run.

$$D = \int_0^L BC_f(\tfrac{1}{2}\rho U^2)dx \qquad (93)$$

The loss in thrust efficiency due to frictional effects can be obtained by dividing this internal drag by the ideal nozzle thrust, F_i:

$$\Delta C_{FG,f} = \frac{D}{F_i} \qquad (94)$$

Including angularity and friction losses, the peak on-design gross thrust efficiency of the nozzle is predicted to be

$$C_{FG}^{pk} = 1 - \Delta C_{FG,\alpha}^{pk} - \Delta C_{FG,f}^{pk} \qquad (95)$$

Nozzle Boundary Layer Development Modeling

In its current state of technology, the science of computational fluid dynamics has evolved to a level of maturity where CFD can be readily applied and results are widely accepted. The advent of modern super computers has resulted in the ability to obtain solutions to the full Navier Stokes Equations that were unimaginable just twenty years ago, leading to detailed boundary layer predictions and an almost unlimited source of flowfield information. While this capability greatly increases the depth of the researcher's toolbox, it also demands an increased commitment; CFD analysis can be time consuming in a first approach, and in many cases, justifies an separate research effort of its own.

For many fluid dynamic applications, methods based on the approximate solution of boundary layer integral conservation laws can yield valid results. These classic methods are simple in derivation, numerical implementation, and application, and have been shown to calculate boundary layer development and skin friction drag with a high degree of accuracy and reliability. In general, however, integral methods are limited to a class of problems in which flow physics are well understood and detailed flowfield information is not required. For basic nozzle geometries, the prediction of nozzle thrust performance is one problem which fits into this category.

Integral methods are based on solutions of the boundary layer integral equation for conservation of momentum, derived physically by von Kármán and mathematically by Polhausen in 1921. The simplest approximate solution to this equation is the well known Kármán-Polhausen Method, used to calculate laminar incompressible flows over a flat plate with zero pressure gradient. Though readily adapted to compressible cases with pressure gradient, laminar methods of this type are not applicable to nozzle flows where Reynolds Numbers are too high for laminar flow to persist, and intense turbulence results in transition Reynolds Numbers that are typically lower than the equivalent flat plate [5].

In 1951, Tucker [6] developed an integral approximation method for calculating the turbulent boundary layer development in compressible flows, and in 1954, Bartz [5] derived a method for calculating the turbulent boundary layer development in axisymmetric rocket nozzles. Both turbulent methods were based on an "analogy" with laminar boundary layer theory; that is, laminar conservation laws were used to derive the basic governing equations. Turbulent boundary layer relations ($u/U=f(y/\delta)$, C_f, etc.) were then imposed on the laminar model to come up with an analogous turbulent boundary layer model. Though Tucker was able to verify results from this model with experimental boundary layer development data, neither author attempted to make or validate skin friction drag calculations, possibly due to a lack of suitable data. The following is an extension of the approximate integral momentum method to a non-axisymmetric, two-dimensional nozzle for the calculation of turbulent boundary layer development and internal performance losses due to skin friction drag.

The Kármán-Polhausen integral boundary layer equation for steady flow conservation of x-momentum is presented in (96), where the x and y axes are the local directions along and normal to the solid boundary [7].

$$\frac{\partial}{\partial x}\int_0^{\delta}\tilde{\rho}u^2\,dy \;-\; U\frac{\partial}{\partial x}\int_0^{\delta}\tilde{\rho}u\,dy \;+\; \int_0^{\delta}\frac{\partial P}{\partial x}\,dy \;=\; -\mu\left[\frac{\partial u}{\partial y}\right]_{y=0} \tag{96}$$

Note that in the following analysis, u is the boundary layer velocity, U is the freestream or edge velocity, $\tilde{\rho}$ is the boundary layer density, ρ is the freestream density, and P is the freestream pressure, henceforth assumed constant in y through a laminar boundary layer analogy. As part of this model, flow outside the boundary layer is assumed isentropic and 1D. For this flow, the Euler Equation for conservation of momentum along a streamline can be written as follows [8]:

$$-\frac{dP}{dx} = \rho U\frac{dU}{dx} \tag{97}$$

The outer pressure gradient can be imposed on the boundary layer model by substituting (97) into the integral momentum equation:

$$\frac{\partial}{\partial x}\int_0^{\delta}\tilde{\rho}u^2\,dy \;-\; U\frac{\partial}{\partial x}\int_0^{\delta}\tilde{\rho}u\,dy \;-\; \rho U\frac{\partial U}{\partial x}\int_0^{\delta}dy \;=\; -\mu\left[\frac{\partial u}{\partial y}\right]_{y=0} \tag{98}$$

Combining terms under the integral results in

$$\int_0^{\delta}\left\{\frac{\partial\tilde{\rho}u^2}{\partial x} - U\frac{\partial\tilde{\rho}u}{\partial x} - \rho U\frac{\partial U}{\partial x}\right\}dy \;=\; -\mu\left[\frac{\partial u}{\partial y}\right]_{y=0} \tag{99}$$

Next, using the product rule to make the following expansion,

$$\frac{\partial\tilde{\rho}u}{\partial x} = \frac{1}{u}\frac{\partial\tilde{\rho}u^2}{\partial x} - \tilde{\rho}\frac{\partial u}{\partial x} \tag{100}$$

the bracketed terms in (99) become:

$$\{\;\} = -\frac{\partial}{\partial x}\left[\rho U^2\frac{\tilde{\rho}u}{\rho U}\left(1-\frac{u}{U}\right)\right] - \rho U\left[1-\frac{\tilde{\rho}}{\rho}\frac{u}{U}\right]\frac{\partial U}{\partial x} \tag{101}$$

Now, use of the product rule to expand the first bracketed term in (101) results in

$$\{\ \} = -\left[\frac{\tilde{\rho}u}{\rho U}\left(1-\frac{u}{U}\right)\frac{\partial \rho U^2}{\partial x} + \rho U^2 \frac{\partial}{\partial x}\left(\frac{\tilde{\rho}u}{\rho U}\left(1-\frac{u}{U}\right)\right)\right] - \rho U \frac{\partial U}{\partial x}\left[1-\frac{\tilde{\rho}}{\rho}\frac{u}{U}\right] \quad (102)$$

Substitution back into the integral momentum equation nets

$$\frac{\partial \rho U^2}{\partial x}\int_0^{\delta}\frac{\tilde{\rho}u}{\rho U}\left(1-\frac{u}{U}\right)dy \ + \ \rho U^2 \frac{\partial}{\partial x}\int_0^{\delta}\left[\frac{\tilde{\rho}u}{\rho U}\left(1-\frac{u}{U}\right)\right]dy$$

$$+ \ \rho U \frac{\partial U}{\partial x}\int_0^{\delta}\left[1-\frac{\tilde{\rho}}{\rho}\frac{u}{U}\right]dy \ = \ \mu\left[\frac{\partial u}{\partial y}\right]_{y=0}$$

Making use of the following definitions for the boundary layer momentum thickness, boundary layer displacement thickness, and wall shear stress [7]:

$$\theta = \int_0^{\delta}\frac{\tilde{\rho}u}{\rho U}\left(1-\frac{u}{U}\right)dy \quad (104)$$

$$\delta^* = \int_0^{\delta}\left[1-\frac{\tilde{\rho}u}{\rho U}\right]dy \quad (105)$$

$$\tau_o = \mu\left[\frac{\partial u}{\partial y}\right]_{y=0} \quad (106)$$

the boundary layer integral momentum equation reduces to:

$$\frac{\partial \rho U^2}{\partial x}\theta + \rho U^2 \frac{\partial \theta}{\partial x} + \rho U \frac{\partial U}{\partial x}\delta^* = \tau_o \quad (107)$$

Dividing through by ρU^2, and noting that [7]

$$C_f = \frac{\tau_o}{\frac{1}{2}\rho U^2} \quad (108)$$

the integral momentum equation can be written as:

$$\frac{\partial\theta}{\partial x}+\theta\left[\frac{1}{\rho U^2}\frac{\partial\rho U^2}{\partial x}+\frac{1}{U}\frac{\partial U}{\partial x}\left(\frac{\delta^*}{\theta}\right)\right]=\frac{C_f}{2} \tag{109}$$

Finally, since $\theta=\theta(x)$, $U=U(x)$, and $\rho U^2=\rho U^2(x)$, $\partial/\partial x$ becomes d/dx and (109) is:

$$\frac{d\theta}{dx}+\theta\left[\frac{1}{\rho U^2}\frac{d\rho U^2}{dx}+\frac{1}{U}\frac{dU}{dx}\left(\frac{\delta^*}{\theta}\right)\right]=\frac{C_f}{2} \tag{110}$$

Equation (110) can be put into a simpler form by noting that, from 1D gas dynamics, with $M=U/a$ as the freestream Mach number [5],

$$d\rho U^2=\rho U^2(2-\gamma M^2)\frac{dU}{U} \tag{111}$$

$$\frac{dU}{U}=\frac{-1}{(1-M^2)}d\left(\ln\frac{A}{A^*}\right) \tag{112}$$

Substitution results in

$$\frac{d\theta}{dx}+\theta\left[\frac{\gamma M^2-\delta^*/\theta-2}{1-M^2}\right]\frac{d}{dx}\left(\ln\frac{A}{A^*}\right)=\frac{C_f}{2} \tag{113}$$

Results obtained up to this point are based on laminar boundary layer theory. To extend this model to an "analogous" turbulent boundary layer, a fully developed turbulent boundary layer with a 1/7-th power law similarity velocity profile ($u/U=(y/\delta)^{1/7}$) and a turbulent flat plate skin friction relationship can be assumed. The local nozzle skin friction coefficient can then be determined using a Blasius skin friction equation for a turbulent boundary layer. The Blasius equation given by Eckert [9] is:

$$\frac{C_f}{2}=0.0228\left[\frac{1}{Re_\delta}\right]^{1/4}=0.0228\left[\frac{\mu}{\rho U\delta}\right]^{1/4} \tag{114}$$

For a compressible boundary layer, the dynamic viscosity in (114) is a function of temperature and must be calculated at the surface "wall" temperature. In the case of a heat conducting compressible boundary layer, this would require a simultaneous solution of the boundary layer integral energy equation. For cold nozzle flows, however, the simplifying and reasonable assumption of an adiabatic boundary layer can be made, since subscale nozzle testing is usually performed over a length of time such that temperature equilibrium

between flow and the nozzle wall can be attained. Noting that the freestream and boundary layer temperatures are T and $\tilde{T}$, respectively, and making the additional assumption of a similarity boundary layer temperature profile where $\tilde{T} / T = f(u / U)$, the energy equation can be directly integrated to give [7]

$$\tilde{T} = T + r\frac{\gamma - 1}{2}\left[TM^2 - \tilde{T}\tilde{M}^2\right] \tag{115}$$

where $\tilde{M} = u / \tilde{a}$ is the boundary layer Mach number and r is the boundary layer temperature recovery factor, which accounts for temperature increases through viscous dissipation in the boundary layer. For a compressible turbulent boundary layer with a Prandtl number of 0.72, r is approximately 0.88 [7].

At y=0, $\tilde{M}$=u=0, $\tilde{T} = \tilde{T}_w$, and (115) gives

$$\frac{\tilde{T}_w}{T} = \left(1 + r\frac{\gamma - 1}{2}M^2\right) \tag{116}$$

To relate viscosity to temperature in a compressible flow, Schlicting [7] suggests the use of a simple power law:

$$\frac{\mu_w}{\mu_0} = \left(\frac{\tilde{T}_w}{\tilde{T}_0}\right)^{\omega} = \left(\frac{\tilde{T}_w}{T_0}\right)^{\omega} \tag{117}$$

where values of $\omega \approx 0.75$ showed good agreement with experimental data in the temperature range from 360 to 560 °R. From 1D gas dynamics, local temperature is related to stagnation temperature by [3]

$$\frac{T}{T_0} = \left[1 + \frac{\gamma - 1}{2}M^2\right]^{-1} \tag{118}$$

So,

$$\frac{\mu_w}{\mu_0} = \left(\frac{\tilde{T}_w}{T}\frac{T}{T_0}\right)^{\omega} = \left[\left(1 + r\frac{\gamma - 1}{2}M^2\right)\left(1 + \frac{\gamma - 1}{2}M^2\right)^{-1}\right]^{\omega} \tag{119}$$

Substitution into the skin friction coefficient equation (114) gives

$$\frac{C_f}{2} = 0.0228\sigma\left[\frac{\mu_0}{\rho U \delta}\right]^{1/4} \tag{120}$$

where σ is defined as follows:

$$\sigma = \left[\left(1 + r\frac{\gamma - 1}{2} M^2 \right) \left(1 + \frac{\gamma - 1}{2} M^2 \right)^{-1} \right]^{\omega/4} \tag{121}$$

From the continuity equation,

$$\rho U A = \rho^* U^* A^* \tag{122}$$

which gives the following:

$$\rho U = \rho^* U^* \left(\frac{A^*}{A} \right) \tag{123}$$

leading to the final form of the skin friction coefficient.

$$\frac{C_f}{2} = 0.0228\sigma \left[\frac{\mu_0}{\rho^* U^* \delta} \left(\frac{A}{A^*} \right) \right]^{1/4} \tag{124}$$

Substituting the compressible skin friction equation (124) into the integral momentum equation (113), multiplying that equation by $\theta^{1/4}$ and noting that

$$\theta^{1/4} \frac{d\theta}{dx} = \frac{4}{5} \frac{d\theta^{5/4}}{dx} \tag{125}$$

the result is:

$$\frac{d\theta^{5/4}}{dx} + \frac{5}{4}\theta^{5/4} \left[\frac{\gamma M^2 - \delta^*/\theta - 2}{1 - M^2} \right] \frac{d}{dx}\left(\ln \frac{A}{A^*} \right) = \frac{5}{4}(0.0228)\sigma \left[\left(\frac{\mu_0}{\rho^* U^*} \right) \left(\frac{\theta}{\delta} \right) \left(\frac{A}{A^*} \right) \right]^{1/4} \tag{126}$$

Note that the boundary layer shape factors $H_1=\delta^*/\theta$ and $H_2=\delta/\theta$ are present in the final form of the integral momentum equation. These are evaluated as follows. First, using the ideal gas law with pressure constant through the boundary layer in y, the following can be written:

$$\frac{\tilde{\rho} u}{\rho U} = \frac{T}{\tilde{T}} \frac{u}{U} \tag{127}$$

With this, equation (115) can be used to rewrite the momentum and displacement thickness integrals in (104) and (105) as:

$$\theta = \int_0^{\delta} \frac{\frac{u}{U}\left(1-\frac{u}{U}\right)}{1+r\left(\frac{\gamma-1}{2}\right)M^2\left[1-\left(\frac{u}{U}\right)^2\right]}\,dy \tag{128}$$

and,

$$\delta^* = \int_0^{\delta} \frac{1+r\left(\frac{\gamma-1}{2}\right)M^2\left[1-\left(\frac{u}{U}\right)^2\right]-\frac{u}{U}}{1+r\left(\frac{\gamma-1}{2}\right)M^2\left[1-\left(\frac{u}{U}\right)^2\right]}\,dy \tag{129}$$

Finally, with $u/U=(y/\delta)^{1/7}$, the integrals become:

$$\theta = \int_0^{\delta} \frac{\left(\frac{y}{\delta}\right)^{1/7}\left[1-\left(\frac{y}{\delta}\right)^{1/7}\right]}{1+r\left(\frac{\gamma-1}{2}\right)M^2\left[1-\left(\frac{y}{\delta}\right)^{2/7}\right]}\,dy = \int_0^{\delta} b(y)dy \tag{130}$$

$$\delta^* = \int_0^{\delta} \frac{1+r\left(\frac{\gamma-1}{2}\right)M^2\left[1-\left(\frac{y}{\delta}\right)^{2/7}\right]-\left(\frac{y}{\delta}\right)^{1/7}}{1+r\left(\frac{\gamma-1}{2}\right)M^2\left[1-\left(\frac{y}{\delta}\right)^{2/7}\right]}\,dy = \int_0^{\delta} c(y)dy \tag{131}$$

Due to their complicated form, equations (130) and (131) are best solved using quadrature. For these equations, Simpson's Rule gives:

$$\theta = \frac{\delta}{6}[b(0)+4b(\delta/2)+b(\delta)] = \frac{\frac{2\delta}{3}\left(\frac{1}{2}\right)^{1/7}\left[1-\left(\frac{1}{2}\right)^{1/7}\right]}{1+r\left(\frac{\gamma-1}{2}\right)M^2\left[1-\left(\frac{1}{2}\right)^{2/7}\right]} \tag{132}$$

$$\delta^* = \frac{\delta}{6}[c(0) + 4c(\delta/2) + c(\delta)] = \frac{\delta}{6}\left[1 + 4\left(\frac{1 + r\left(\frac{\gamma-1}{2}\right)M^2\left[1-\left(\frac{1}{2}\right)^{2/7}\right] - \left(\frac{1}{2}\right)^{1/7}}{1 + r\left(\frac{\gamma-1}{2}\right)M^2\left[1-\left(\frac{1}{2}\right)^{2/7}\right]}\right)\right] \tag{133}$$

With the following substitution

$$\lambda = \lambda(x) = 1 + r\left(\frac{\gamma-1}{2}\right)M^2\left[1-\left(\frac{1}{2}\right)^{2/7}\right] \approx 1 + 0.1797\ r\left(\frac{\gamma-1}{2}\right)M^2 \tag{134}$$

the shape factors are:

$$H_1 = \frac{\delta^*}{\theta} = \left(\frac{1}{2}\right)^{-1/7}\left[\frac{5\lambda}{4} - \left(\frac{1}{2}\right)^{1/7}\right]\left[1-\left(\frac{1}{2}\right)^{1/7}\right]^{-1} \approx 14.6390\ \lambda - 10.6071 \tag{135}$$

$$H_2 = \frac{\delta}{\theta} = \frac{3\lambda}{2}\left(\frac{1}{2}\right)^{-1/7}\left[1-\left(\frac{1}{2}\right)^{1/7}\right]^{-1} \approx 17.5668\ \lambda \tag{136}$$

Finally, with the following functional definitions,

$$f(x) = \frac{5}{4}\left[\frac{\gamma M^2 - H_1 - 2}{1 - M^2}\right]\frac{d}{dx}\left(\ln\frac{A}{A^*}\right) \tag{137}$$

$$g(x, NPR) = \frac{5}{4}(0.0228)\sigma\left[\left(\frac{\mu_0}{\rho^* U^*}\right)\left(\frac{1}{H_2}\right)\left(\frac{A}{A^*}\right)\right]^{\frac{1}{4}} \tag{138}$$

$$\Theta = \theta^{5/4} \tag{139}$$

the integral momentum equation can be written in a compact form.

$$\frac{d\Theta}{dx} + f(x)\Theta = g(x, NPR) \tag{140}$$

Equation (140) is a first order, linear, nonhomogeneous ordinary differential equation which sets up an initial value problem when an onset boundary layer momentum thickness is specified. Several different numerical schemes have been used to solve this problem with a similar degree of success, including a multistep backward-space (upwind) finite

difference method, a fourth order Runga-Kutta method, and a fourth order Adams-Bashforth predictor - Adams-Moulton corrector method.

As mentioned at the beginning of this analysis, the pressure gradient used to calculate the boundary layer development is based on the inviscid outer flow. Once an inviscid solution is obtained, the estimated boundary layer displacement thickness can be added to the inviscid wall geometry and the boundary layer calculation iterated upon until a solution is obtained that satisfies both the boundary layer model and the pressure gradients imposed by the boundary layer displacement. Pressure gradient changes due to displacement effects are generally on the order of δ^* itself, so an iterated solution may or may not vary significantly from the initial, inviscid boundary solution, depending on the nozzle geometry and displacement thickness development. However, an iterative procedure of the type discussed is easy to implement and generally converges quite rapidly, so little additional computational work is required to correct for displacement effects.

Code Development and Application

The boundary layer integral momentum method derived above was combined with thrust performance calculations and integrated into a prediction program NPAC, which stands for Nozzle Performance Analysis Code. Results presented in this paper were obtained using a 4th order Runga-Kutta method embedded in an iterative boundary layer displacement correction scheme to solve the integral momentum equation and calculate boundary layer development and skin friction drag. For this study, NPAC was run on a Digital Equipment Corporation Alpha 3000 workstation in interactive mode.

The non-axisymmetric nozzle geometries used in this analysis and the data presented in this discussion originated from sub-scale nozzle testing conducted at the NASA Langley Research Center 16 Foot Transonic Tunnel Complex over the past 20 years. Propulsion test facilities at this complex use a high pressure air supply system with a series of reservoirs, valves, filters, and heat exchangers to provide clean, dry airflow at a constant total temperature of about 530 °R and mass flow rates up to 30 lbm/sec at atmospheric back pressure. Details of a typical propulsion simulation system are shown in Figure 12. Nozzle air flow rates are calculated based on pressure and temperature measurements in a calibrated multiple critical venturi system located upstream of the propulsion simulation model. Forces and moments generated by the nozzle are measured by a six-component strain-gauge balance mounted on the propulsion model centerline and corrected to

calibration standards. Stagnation conditions are measured by pitot pressure rakes and thermocouple probes. Reference [10] provides further details of the test facilities at the 16 Foot Transonic Tunnel Complex.

Figure 12: Propulsion Simulation System

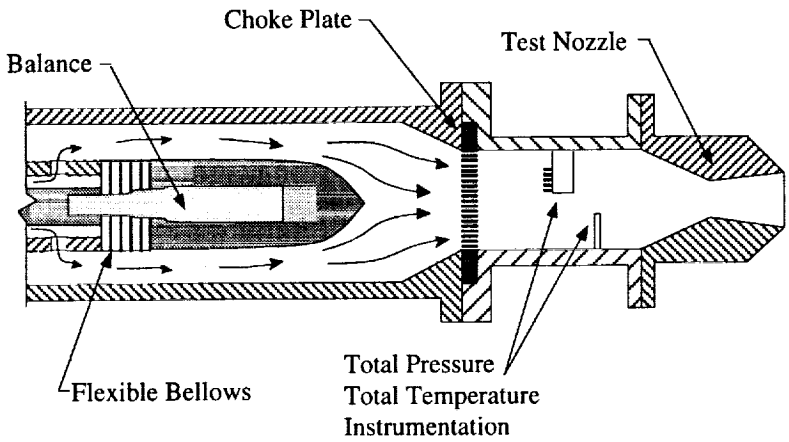

For this discussion, four different nozzles were analyzed and results compared to experimental data to show both the validity and the limitations of NPAC. All nozzles were non-axisymmetric, two-dimensional, convergent-divergent nozzles with nominal throat areas (A_8) ranging from 2.50 to 4.32 in^2 and expansion ratios (A_9/A_8) ranging from 1.09 to 1.80. For analysis, the centerline length of each nozzle was broken down into 2000 intervals of approximately 0.005 in. each in length. Each interval was projected to the nozzle channel contour to determine the local Runga Kutta step size (Δx_i) which was then halved to provide starting (x_i-Δx_i), intermediate (x_i-$\Delta x_i/2$), and calculation (x_i) points for the fourth order Runga Kutta solution. It is important to note that the Runga Kutta solution was largely unaffected by changes in interval size, and that size was chosen primarily to obtain proper resolution of the nozzle geometry for wetted area calculations.

At the appropriate design NPR, boundary layer development calculations were started downstream of the propulsion simulation system choke plate with an assumed zero thickness onset boundary layer. Boundary layer displacement thickness corrections were made to the inviscid nozzle geometry until the boundary layer displacement thickness development converged to machine accuracy. At that point, skin friction drag calculations were made over the full length of the nozzle flaps and sidewalls beginning at the nozzle entrance. The skin friction estimate was combined with the geometric angularity loss calculation to predict the peak gross thrust efficiency of the test nozzle. From that point,

the thermodynamic thrust performance model was used to determine over- and underexpansion effects at off-design nozzle pressure ratios.

Case 1

The nozzle studied in Case 1 was tested by Mason, Putnam, and Re [11], and has a nominal throat area of 4.3106 in^2, a divergence angle of 1.21°, an expansion ratio of 1.09, and a corresponding design NPR of 2.97. Geometry details are shown in Figure 13. This nozzle was used as part of an investigation to determine the effects of throat contouring on 2D-CD nozzle static internal performance.

Figure 13: Case 1 Nozzle Geometry. Dimensions in inches.

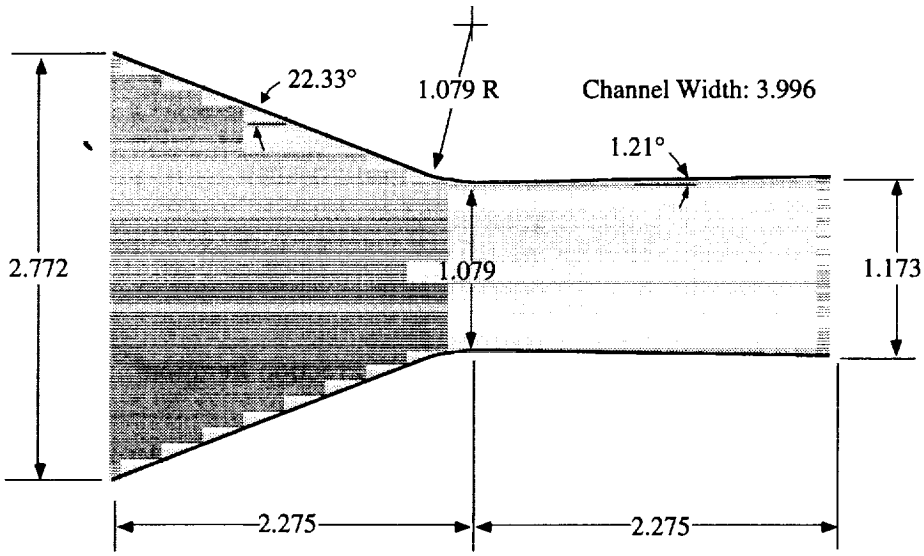

The calculated boundary layer development for this nozzle is presented in Figure 14 after one iteration (inviscid pressure gradient), and after the last iteration (displacement corrected pressure gradient). The only difference in the boundary layer development in the two cases is at the nozzle entrance, where the corrected pressure gradient resulted in a slightly thinner boundary layer due to displacement effects in the subsonic "flat plate" instrumentation section upstream of the test nozzle. This initial difference is seen to be of no consequence further downstream, where the boundary layer development is the same for the inviscid and corrected cases. As observed by Bartz [5], the nozzle boundary layer reaches a minimum thickness slightly upstream of the nozzle throat and growth in the divergent section of the nozzle is nearly linear. Other nozzle cases investigated in this analysis displayed similar boundary layer development.

Figure 14: Calculated Turbulent Boundary Layer Development for Case 1.

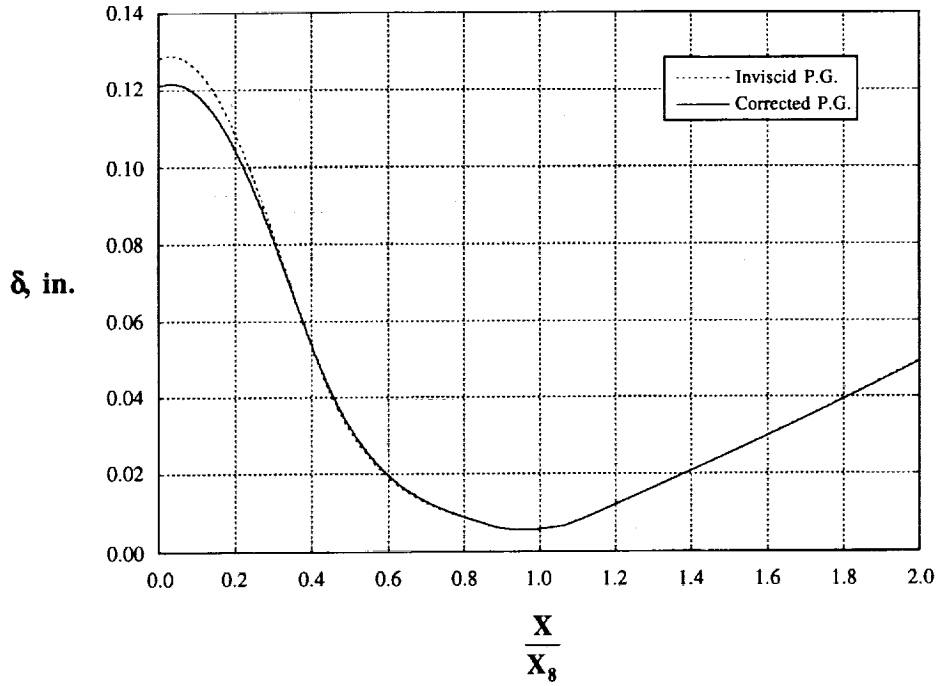

Figure 15: Convergence of δ* Development under the Correction Iteration

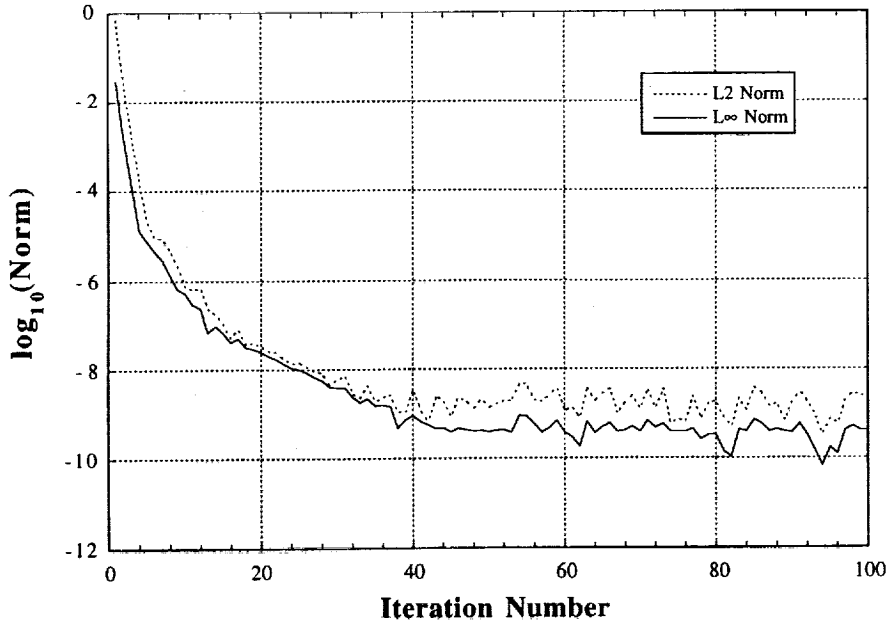

Convergence of the boundary layer displacement thickness development under the iterative correction scheme is shown in Figure 15, where L_∞ and L_2 norms of the residual vector are plotted against iteration number. Note that the residual vector consists of components representing the residual at each calculation point along the nozzle length. The correction scheme is seen to converge to machine accuracy in less than 50 iterations. Other nozzle cases discussed in this paper displayed similar convergence behavior.

The gross thrust efficiency prediction for the Case 1 nozzle is compared to experimental data in Figure 16 and shows excellent agreement throughout the NPR range tested. Peak thrust efficiency was predicted to within 0.1 percent, and the NPAC prediction agrees with all data to within the measurement system precision (about 0.5 percent). Losses predicted by NPAC at peak were as follows: $\Delta C_{FG,f}$=0.011, $\Delta C_{FG,\alpha} \approx 0$.

Figure 16: Predicted and Experimental [11] Thrust Efficiency for Case 1

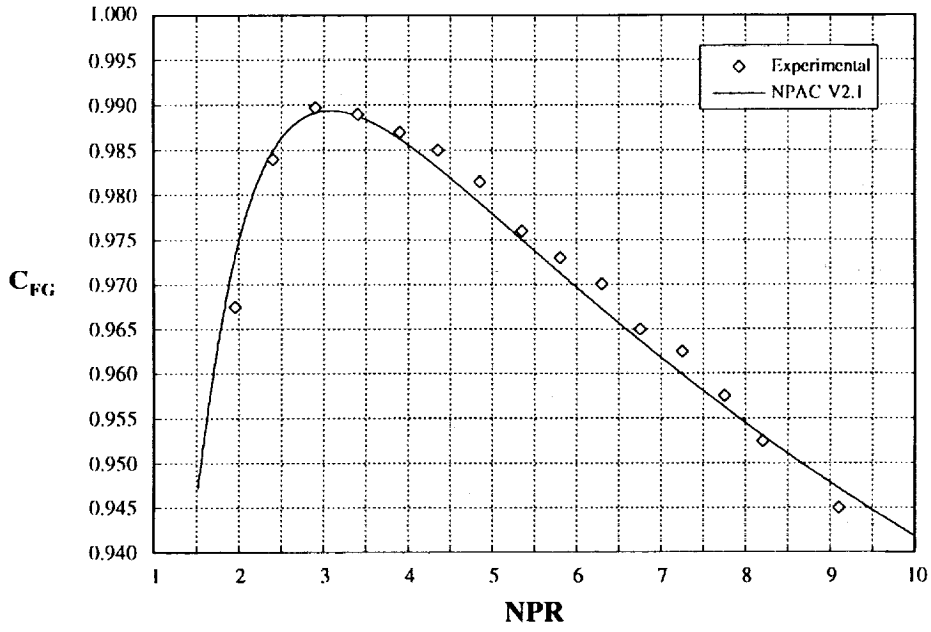

Case 2

Experimental results for the 2D-CD nozzle investigated in Case 2 are discussed by Berrier and Re in [12]. As shown in Figure 17, this nozzle has a nominal throat area of 4.3262 in^2, a divergence angle of 5.38°, an expansion ratio of 1.25, and a corresponding design NPR of 4.22. This particular nozzle was used as part of a test program to evaluate the effects of several geometric parameters on nozzle internal performance.

Figure 17: Case 2 Nozzle Geometry. Dimensions in inches.

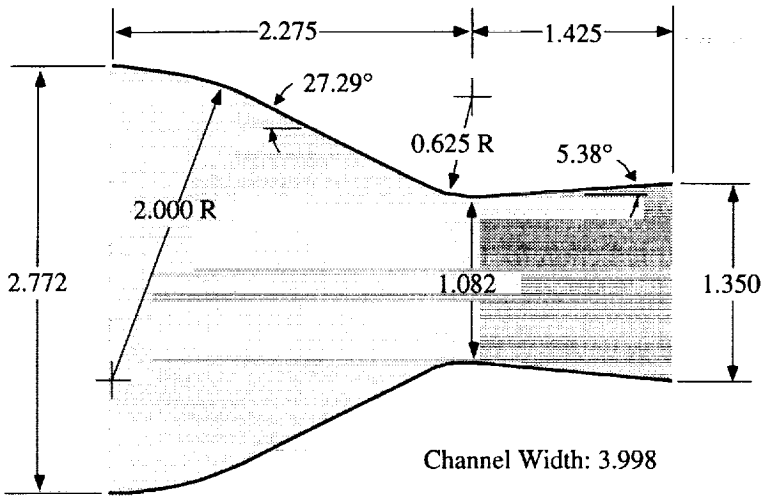

For Case 2, the gross thrust efficiency prediction is compared to experimental data in Figure 18. Once again, there is good agreement throughout the NPR range shown, and peak thrust efficiency fell between repeat experimental data points at NPR=4.25. For this nozzle, NPAC predicted a peak gross thrust efficiency of 0.991, with a loss breakdown of $\Delta C_{FG,f}$=0.007 and $\Delta C_{FG,\alpha}$=0.002.

Figure 18: Predicted and Experimental [12] Thrust Efficiency for Case 2

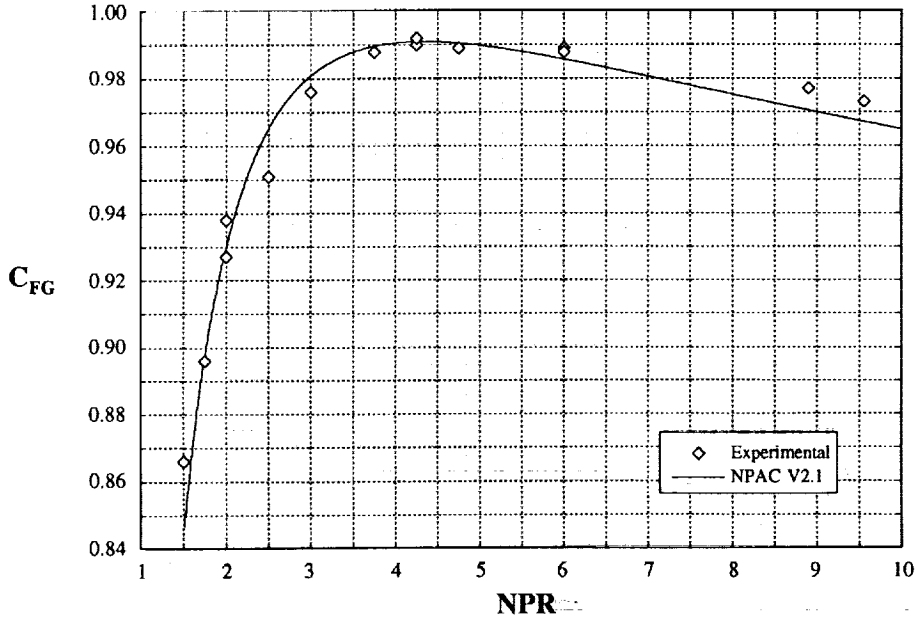

Case 3

The nozzle used in Case 3 has a nominal throat area of 4.3172 in^2, an expansion ratio of 1.797, a corresponding design pressure ratio of 8.78, and a steep divergent flap angle of 11.01°. This nozzle was tested by Hunter [13] to investigate passive shock - boundary layer interaction control concepts. Specific details of the nozzle internal geometry are presented in Figure 19.

Figure 19: Case 3 Nozzle Geometry. Dimensions in inches.

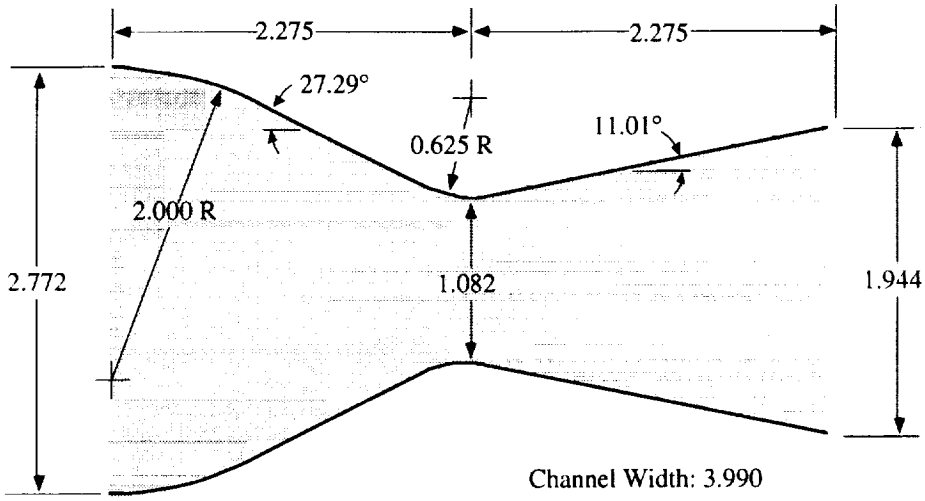

Unlike previous cases, the thrust efficiency prediction for Case 3 in Figure 20 shows less favorable agreement with experimental data over the entire NPR range tested. NPAC did predict the peak gross thrust efficiency coefficient and modeled off-design performance almost exactly down to NPR= 5.0. Below this NPR, though, the measured gross thrust efficiency rose higher than the NPAC prediction, and the difference increased at lower NPR's. Such behavior might seem puzzling at first, since losses measured at the design NPR should not change at off-design high end NPR's, and would certainly not decrease at the rate seen in experimental data. As discussed earlier, however, one mechanism can significantly alter off-design nozzle performance and would increase thrust efficiency: boundary layer separation. Experimental off-design internal pressure data for the Case 3 nozzle are presented in Figure 21, and show strong evidence of shock induced separation with little or no downstream static pressure recovery in the divergent section of the nozzle for NPR's between 1.8 and 5.0. Above NPR=5.0, the nozzle was shock free, and thus was performing as the NPAC model would predict.

Figure 20: Predicted and Experimental [13] Thrust Efficiency for Case 3

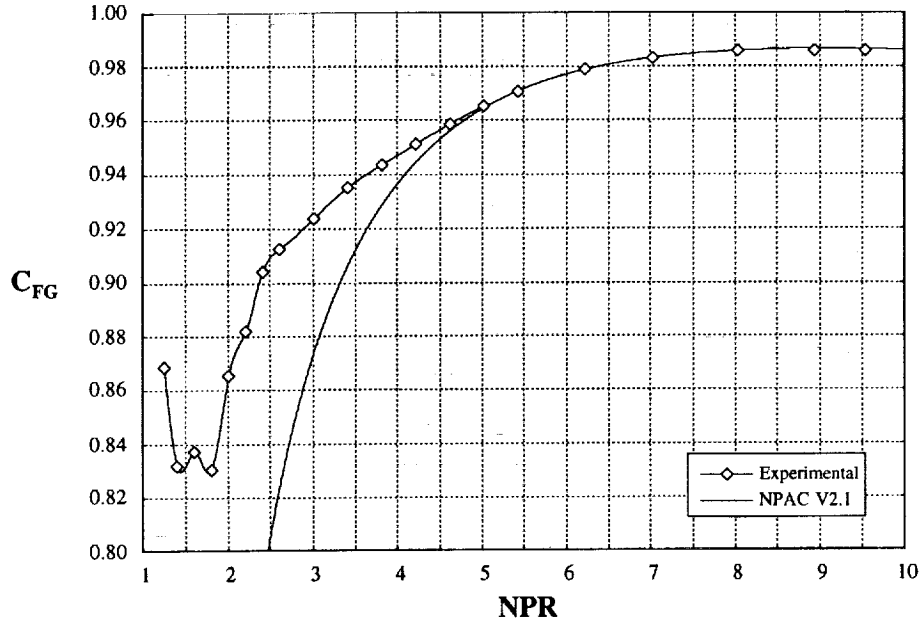

Figure 21: Experimental Off-Design Pressure Data for Case 3 [13]

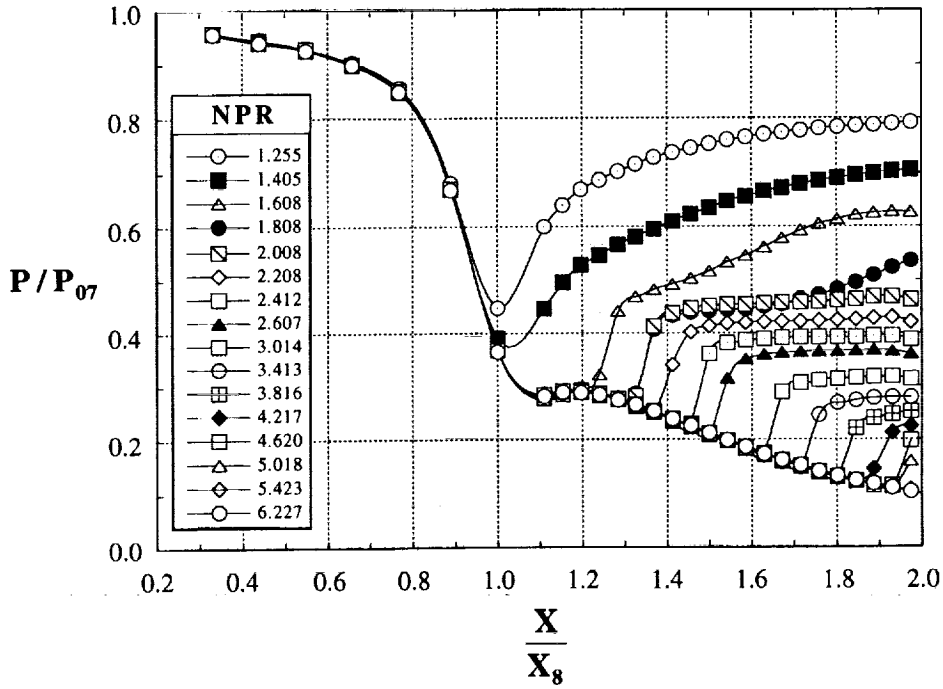

It is interesting to note that between NPR's 1.8 and 2.4, experimental gross thrust efficiency data followed the same trend as the NPAC prediction, though it was shifted to lower NPR's by $\Delta NPR \approx 1.0$. This supports the notion of an NPR range shift discussed previously, and indicates that a large portion of that shift occurs at lower NPR's, where the nozzle shock is further upstream and more dramatic changes in the effective nozzle geometry can occur through separation.

Note that for Case 3, the predicted gross thrust efficiency at peak was 0.986, with associated losses of $\Delta C_{FG,f}=0.008$ and $\Delta C_{FG,\alpha}=0.006$.

Case 4

The final nozzle studied in this analysis was tested by Capone and Berrier [14] as part of a wind tunnel experiment on a 1/10-scale, twin engine F-18 prototype aircraft model, and is a 2D-CD nozzle with an expansion ratio of 1.15, a design NPR of 3.46, and a nominal throat area of 2.50 in^2. Details of the nozzle geometry are presented in Figure 22. Note that this nozzle had a cutback outside sidewall and an extended nozzle inter-fairing on the inside sidewall, and thus was not truly a 2D nozzle along its entire length. The geometry shown in Figure 22 is defined by the nozzle upper and lower flaps and does not take sidewall variations into account.

Figure 22: Case 4 Nozzle Geometry. Dimensions in inches.

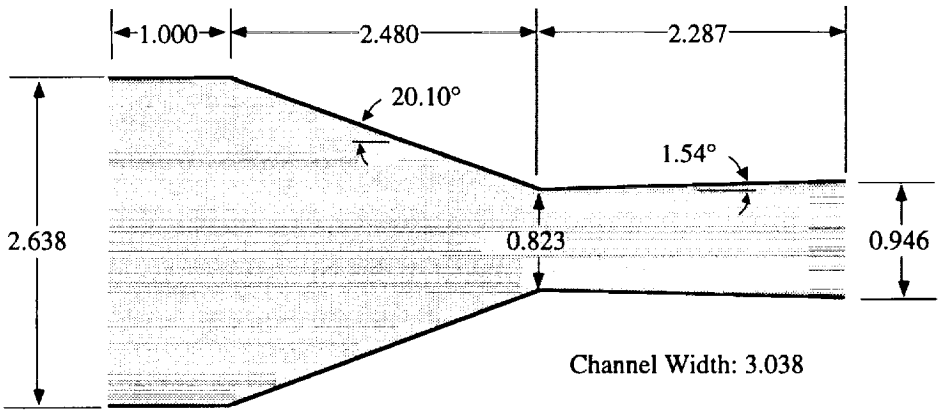

The thrust efficiency prediction for this nozzle is shown compared to experimental data in Figure 23. In this last case, the NPAC prediction does not match experimental data very well. Most of the thrust efficiency data at and below design is within a 0.5 percent measurement system precision band around the NPAC prediction, but previous cases have

demonstrated that agreement should be much better than that quoted limit. In addition, experimental gross thrust efficiency was much higher than the NPAC prediction at underexpanded NPR's. Regardless of exact levels, however, there is a notable NPR shift between the NPAC thrust performance curve and experimental data over the entire NPR range tested, and a closer look at the data shows that the nozzle reached a peak thrust performance level at about NPR=4.5, approximately 1 NPR higher than the ideal peak. It is apparent that physics outside of the realm of the NPAC gas dynamics / integral momentum boundary layer model were present in this case.

Figure 23: Predicted and Experimental [14] Thrust Efficiency for Case 4

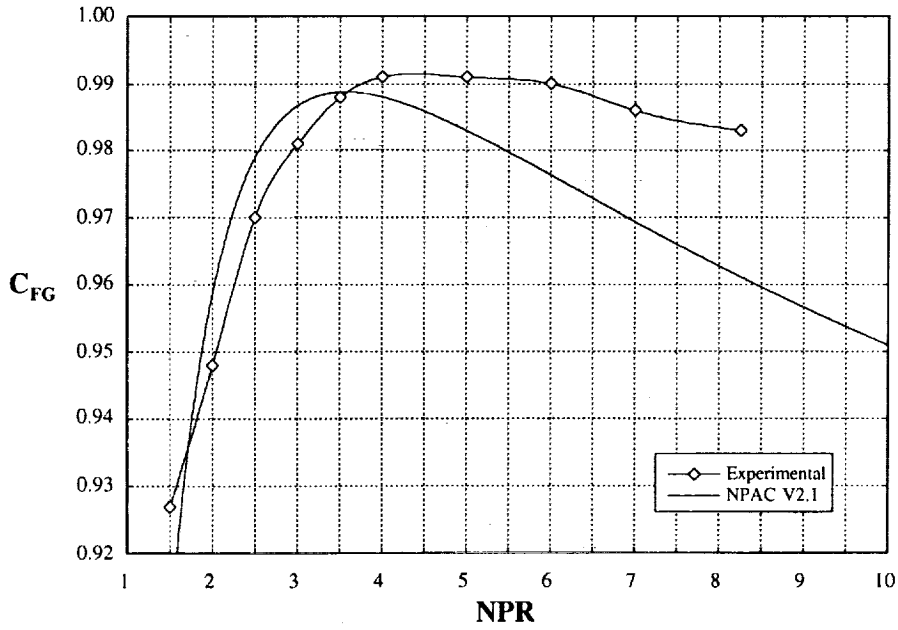

The flow physics missing from the NPAC model in this last case can be linked to two relatively simple factors: the cutback outside sidewall, and the twin engine configuration. The cutback sidewall would have the effect of increasing the effective expansion ratio of the nozzle and shifting peak performance to a higher NPR, while the twin engine configuration would cause interaction effects between the two nozzle jets. Because of the complicated jet plume structure at above-design underexpanded NPR's, interaction effects are intense in this range and can result in a dynamic "coupling" of the two jets, in which case the twin jet configuration behaves much differently than two isolated single jets. Though this mechanism generally increases thrust efficiency, it can result in stability and aeroacoustic fatigue problems.

Conclusions

In this paper, the basic flow physics and thrust performance characteristics of convergent-divergent exhaust nozzles were discussed. From this point, thermodynamic relations governing nozzle internal performance were derived using one-dimensional gas dynamics, and an approximate integral momentum boundary layer method was developed based on the classic Kármán-Polhausen solution to calculate boundary layer development and skin friction losses. Together with angularity effects, these models were written into a computational code (NPAC), and used to predict the static thrust performance of 2D-CD nozzles. To demonstrate the prediction method, computational results were compared to experimental data in four case studies. Important conclusions are as follows.

1. The NPAC method showed excellent agreement with experimental data in predicting the peak gross thrust efficiency of 2D-CD nozzles for basic 2D geometries (three out of the four cases studied to within 0.1 percent). This leads to an important follow-on conclusion relating the physics of nozzle internal flows to the physics represented in the NPAC model; namely, losses in 2D-CD nozzles are due primarily to skin friction and angularity. Two-dimensional nozzles are generally acknowledged to have lower peak gross thrust efficiencies than axisymmetric nozzles of the same expansion ratio and throat area, but in the past, the general hypothesis has been to attribute these additional losses to the existence of corner flows. The current analysis suggests that these secondary flows, if they exist, have a minor effect on thrust performance, and indicates that lower peak gross thrust efficiencies seen in 2D nozzles are most likely due to an increase in wetted area (for the same 1D flow area, a square duct has approximately 1.13 times more wetted perimeter than a circular duct).

2. For low expansion ratio nozzles (A_9/A_8=1.09, 1.25) with shallow divergence angles (α=1.2°, 5.4°), the NPAC thrust performance prediction showed excellent agreement with experimental data throughout the entire NPR range. Differences between the predicted gross thrust efficiency and experimental data were generally well within the approximate 0.5 percent precision limit of the experimental measurement system.

3. The NPAC gross thrust efficiency prediction matched experimental data almost exactly for a high expansion ratio nozzle (A_9/A_8=1.80) with a steep divergence angle (α=11°) from underexpanded conditions down to overexpanded NPR's at which internal shock induced boundary layer separation began to affect nozzle performance. The separation had a notable impact on nozzle performance, and resulted in a significant increase in off-design gross thrust efficiency over what the thermodynamic model predicted.

4. For a twin jet configuration with cutback outside nozzle sidewalls and an extended nozzle inter-fairing, the flow physics and nozzle geometry assumptions represented in the NPAC model were not suitable to correctly predict nozzle thrust performance. The quasi-2D nozzle geometry and dynamic coupling of the two jets resulted in different thrust performance characteristics than would be predicted for an isolated 2D nozzle.

From these conclusions, some important points can be made. First, the NPAC model can accurately predict the static internal thrust performance of basic, isolated 2D-CD nozzles. For cases in which shock induced boundary layer separation dominates off-design performance, the NPAC prediction cannot account for separation effects, but is valid for externally overexpanded, design, and underexpanded NPR's. Though these two points define the basic capabilities and limitations of the NPAC method, they in no way impose limitations on its application. As was seen in this discussion, one of the most powerful uses of the NPAC method lies in interpreting experimental data. By fully understanding the fluid mechanics, thermodynamics, loss effects, and physics represented in the NPAC model, a comparison of the NPAC prediction with experimental data can lend valuable insight into the fundamentals of nozzle thrust performance, and can help explain why a particular nozzle might perform as it does. So, disagreement between the NPAC prediction and experimental data in some cases may be as valuable as agreement in other cases.

Though NPAC is not meant to compete with more powerful CFD codes, the NPAC method is a feasible alternative for nozzle performance modeling when only thrust efficiency or boundary layer development predictions are necessary. In some cases, the simplicity, ease of implementation, and quick convergence of NPAC may make this a more suitable analysis method. In any event, NPAC is a good companion analysis tool to CFD codes both as a fundamental prediction method for interpreting CFD results, and also as a stand alone, independent fluid dynamic model.

References

[1] Stitt, L.E. "Exhaust Nozzles for Propulsion Systems With Emphasis on Supersonic Cruise Aircraft". NASA Reference Publication 1235, May 1990.

[2] Carlson, J.R. "A Nozzle Internal Performance Prediction Method" NASA TP 3221, October 1992.

[3] Liepmann, H.W., and Roshko, A. Elements of Gasdynamics. New York: John Wiley & Sons, 1957.

[4] Zucker, R.D. Fundamentals of Gas Dynamics. Chesterland, OH: Matrix Publishers, 1977.

[5] Bartz, D.R. "An Approximate Solution of Compressible Turbulent Boundary-Layer Development and Convective Heat Transfer in Convergent-Divergent Nozzles". ASME Paper 54-A-153, 1954.

[6] Tucker, M. "Approximate Calculation of Turbulent Boundary-Layer Development in Compressible Flow". NACA Technical Note 2337, April 1951.

[7] Schlicting, H. Boundary Layer Theory. New York: McGraw-Hill, 1979.

[8] Yih, C-S. Fluid Mechanics. Ann Arbor: West River Press, 1977.

[9] Eckert, E.R.G. Introduction to the Transfer of Heat and Mass. New York: McGraw-Hill, 1950.

[10] Staff of the Propulsion Aerodynamics Branch. "A User's Guide to the Langley 16-Foot Transonic Tunnel Complex". NASA TM 102750, September 1990.

[11] Mason, M.L., Putnam, L.E., and Re, R.J. "The Effect of Throat Contouring on Two-Dimensional Converging-Diverging Nozzles at Static Conditions". NASA TP 1704, August 1980.

[12] Berrier, B.L., and Re, R.J. "Effects of Several Geometric Parameters on the Static Internal Performance of Three Nonaxisymmetric Nozzle Concepts". NASA Technical Paper 1468, July 1979.

[13] Hunter, C.A. "An Experimental Analysis of Passive Shock - Boundary Layer Interaction Control for Improving the Off-Design Performance of Jet Exhaust Nozzles". M.S. Thesis, George Washington University, September 1993.

[14] Capone, F.J., and Berrier, B.L. Investigation of Axisymmetric and Nonaxisymmetric Nozzles Installed on a 0.10-Scale F-18 Prototype Airplane Model". NASA TP 1638, June 1980.

REPORT DOCUMENTATION PAGE

Form Approved
OMB No. 0704-0188

Public reporting burden for this collection of information is estimated to average 1 hour per response, including the time for reviewing instructions, searching existing data sources, gathering and maintaining the data needed, and completing and reviewing the collection of information. Send comments regarding this burden estimate or any other aspect of this collection of information, including suggestions for reducing this burden, to Washington Headquarters Services, Directorate for Information Operations and Reports, 1215 Jefferson Davis Highway, Suite 1204, Arlington, VA 22202-4302, and to the Office of Management and Budget, Paperwork Reduction Project (0704-0188), Washington, DC 20503.

1. AGENCY USE ONLY *(Leave blank)*	2. REPORT DATE	3. REPORT TYPE AND DATES COVERED
	March 1995	Contractor Report

4. TITLE AND SUBTITLE
An Approximate Theoretical Method for Modeling the Static Thrust Performance of Non-axisymmetric Two-Dimensional Convergent-Divergent Nozzles

5. FUNDING NUMBERS
NCC1-14
NCC1-24
537-07-20

6. AUTHOR(S)
Craig A. Hunter

7. PERFORMING ORGANIZATION NAME(S) AND ADDRESS(ES)
George Washington University / JIAFS
NASA Langley Research Center
Hampton, VA 23681-0001

8. PERFORMING ORGANIZATION REPORT NUMBER

9. SPONSORING / MONITORING AGENCY NAME(S) AND ADDRESS(ES)
National Aeronautics and Space Administration
Langley Research Center
Hampton, VA 23681-0001

10. SPONSORING / MONITORING AGENCY REPORT NUMBER
NASA CR-195050

11. SUPPLEMENTARY NOTES
This research was part of a thesis program conducted in partial fulfillment of the Master of Science degree from The George Washington University. Langley Technical Monitor: Bobby L. Berrier.

12a. DISTRIBUTION / AVAILABILITY STATEMENT
Unclassified - Unlimited
Subject Category 02

12b. DISTRIBUTION CODE

13. ABSTRACT *(Maximum 200 words)*

An analytical/numerical method has been developed to predict the static thrust performance of non-axisymmetric, two-dimensional convergent-divergent exhaust nozzles. Thermodynamic nozzle performance effects due to over- and underexpansion are modeled using one-dimensional compressible flow theory. Boundary layer development and skin friction losses are calculated using an approximate integral momentum method based on the classic Kármán-Polhausen solution. Angularity effects are included with these two models in a computational Nozzle Performance Analysis Code, NPAC. In four different case studies, results from NPAC are compared to experimental data obtained from subscale nozzle testing to demonstrate the capabilities and limitations of the NPAC method. In several cases, the NPAC prediction matched experimental gross thrust efficiency data to within 0.1 percent at a design NPR, and to within 0.5 percent at off-design conditions.

14. SUBJECT TERMS
Non-axisymmetric Nozzles, Static Thrust Performance, Approximate Theoretical Prediction Method, Comparison with Experimental Data.

15. NUMBER OF PAGES
50

16. PRICE CODE
A03

17. SECURITY CLASSIFICATION OF REPORT	18. SECURITY CLASSIFICATION OF THIS PAGE	19. SECURITY CLASSIFICATION OF ABSTRACT	20. LIMITATION OF ABSTRACT
Unclassified	Unclassified	Unclassified	